Study of Preformed Particle Gel Blocking Performance in Fractured Carbonate Reservoirs

Dongqing Cao, Dr. Ayman M. Almohsin, Dr. Ming Han and Dr. Bader G. Alharbi

Abstract /

The blocking capacity of a preformed particle gel (PPG) in fractures is critical for a water shutoff application in fractured reservoirs. This work studies the PPG blocking behavior by a series of coreflooding tests in fractured carbonate cores. The effects of PPG strengths, PPG pack density, and particle/fracture size ratio were systematically investigated.

Four PPG samples, named HOP-1, HOP-2, HOP-3, and HOP-4, with similar dry particle sizes were used in the work. The swelling ratio of the PPG samples in different salinity brines was tested. The strength of the swollen PPGs was measured by a rheometer. The blocking capacity was tested by injecting water into a PPG packed open fracture core. The differential pressure of water injection was monitored.

The average particle sizes of the dry PPG samples were all around 0.5 mm. The swelling capacities of PPG showed a reverse correlation with brine salinity. The swelling ratio presented an order of HOP-1 > HOP-2 > HOP-3 > HOP-4. Correspondingly, the storage modulus of the four samples increased from a magnitude of 2,000 Pa to 14,000 Pa, and the average particle size decreased from 2.4 mm to 1.1 mm.

The blocking performance of the PPG pack in the fracture depended on the tolerance to water. The PPG samples presented better blocking in smaller sized fractures. A firm pack could dramatically improve the blocking to the fracture. The strength of the PPG sample affected the PPG blocking behavior significantly. HOP-3 showed better performance than the other samples due to the well-adjusted properties in blocking and flow tolerance.

This study explores the matching relationship between the PPG strength, size, and fracture width, which is beneficial for selecting a proper PPG sample for fractured carbonate reservoirs.

Introduction

Gel treatment is a widely used technology for conformance control, water shutoff, and in-depth fluid diversion in heterogeneous reservoirs[1-3]. The traditional in situ gel treatment is engaged in injecting a gelant — composed of a polymer and crosslinker — solution into reservoir formations to make gelation occur in the proper location to divert the subsequent water flow. It has some drawbacks in this kind of treatment, such as lack of gelation time control, uncertainness of gelation due to shear, caused by chromatographic separation, dilution, and dispersion of the components in the gelant[4].

The trend for gel treatment in the industry is applying a preformed particle gel (PPG)[5-7]. Initialed in late 1990s, the PPG technology has been successfully used in China for more than 5,000 wells to reduce water production in mature waterflooded areas[8].

PPGs are polymeric gel particles formed on the surface before injection into the reservoir. When dispersed in an aqueous solution, PPGs absorb water, up to hundreds of times the original dry PPG volume, and do not dissolve. The swollen PPGs are elastic and deformable. With the particle size adjustable from micrometer to centimeter, PPGs are usually applied in the reservoirs with fractures or high permeability flow channels. After injection into the reservoir formations, PPGs preferentially enter the fractures and form a gel pack, which reduces the subsequent fluid flow in the fracture and diverts the flow to the adjacent matrix.

Much research has been conducted to study the PPG blocking performance in porous media and fractures. Bai et al. (2007)[9] and Zhang and Bai (2011)[10] studied the flow mechanisms of PPG in porous media and open fractures. The micromodel and coreflooding experiments showed that a swollen PPG particle could pass through a pore throat with a diameter smaller than the particle, owing to the elasticity and deformability. During injection into the open fracture, PPG propagated like a piston along a fracture and a gel pack was formed in the fracture. The post-water injection could break through the particle gel pack by channels created by the injected water.

Imqam et al. (2015)[11] examined the effect of the fracture's inner diameter and the PPG strength on the injectivity index, resistance factor, and blocking efficiency. The results reported that weak gel had less injection pressure at a large particle/opening ratio compared to a strong gel. The PPG strength affected injectivity more significantly than the particle/fracture size ratio did. The PPG's plugging efficiency depended highly on the particle strength and the conduit's inner diameter. The PPG's injection and placement mechanism through Super-K permeability

cores were reported[12], which showed that the PPGs in-depth permeability reduction to the cores relied on the PPG size, strength, concentration, and sand permeability.

Imqam et al. (2016)[13] and (2017)[14] also investigated the influence of some key factors on gel injectivity and plugging performance for water flow through opening fractures. Results from single uniform fracture experiments showed that the PPG injection pressure was more sensitive to gel strength than gel particle size. Results from single heterogeneous fracture model experiments showed that the PPG injection pressure increased as the fracture heterogeneity in sections increased.

Wang and Bai (2018)[15] investigated the PPG placement and plugging in partially open fractures. In the fractures with tips, the PPG injection pressure increased rapidly. The blocking efficiency to water showed a growth with the increase of placing pressure. Wu et al. (2018)[16] studied the matching between PPG size and reservoir heterogeneity using a heterogeneous parallel dual sand pack experimental setup. The matched PPG mesh increased as the permeability ratio of the heterogeneous sand pack increased.

In this work, the factors of PPG strength and particle size were studied by testing the blocking performance of the gel pack in the fractures. The bulk properties of four PPG samples were evaluated. A series of coreflooding tests were conducted on the fractured nature carbonate cores.

Experimental

PPG Samples

Four PPG samples with similar initial dry particle sizes were used in the tests. All samples were in the form of dry particulate. Some basic information of these PPGs are listed in Table 1.

Brines

Three kinds of brines were used in the PPG evaluation, including two types of injection water; injection water 1, injection water 2, and connate water. The salinities (total dissolved solids) were 1,317 mg/L, 2,425 mg/L, and 237,959 mg/L, respectively. The ion composition of the brines is listed in Table 2.

Core Plugs

The cylindrical carbonate outcrops were used to make fractures. Table 3 shows the basic properties of the cores. The gas permeabilities of the core samples were all around 50 md. Because the cores were cut before saturating with brine, the brine permeability was not tested. From the result of the similar core sample, the value was about 35 md.

Swelling Ratio Measurement

The swelling ratio of the PPGs was tested by reading the apparent volume before and after the swelling in the brines. A given weight of the dry PPG sample was put in a measuring cylinder. Then, a quantitative volume of brine was added into the cylinder. The sample was allowed to swell completely overnight, and the apparent volume was recorded.

Strength Measurement

The strength of the swollen particles was measured using a remoter (TA Discovery II). A dynamic strain sweep test was first performed to determine the range of linear

Table 1 *Some basic information of the PPG samples used in the tests.*

PPG Sample	Absorption Deionized Water (g/g)	Apparent Powder Density (g/ml)	Moisture Content (%)	pH in ID Water	Initial Particle Size (mm)
HOP-1	46.40	1	10.36	6-7	0.426
HOP-2	30.84	0.95	5.08	6-7	0.524
HOP-3	4.96	0.96	3.48	6-7	0.444
HOP-4	5.08	0.95	11.39	6-7	0.404

Table 2 *The composition of the brines used in the PPG evaluation.*

Brine/Ion	Na^+ (mg/L)	Ca^{2+} (mg/L)	Mg^{2+} (mg/L)	Ba^{2+} (mg/L)	K^+ (mg/L)	Cl^- (mg/L)	HCO_3^- (mg/L)	SO_4^{2-} (mg/L)	TDS (mg/L)
Injection Water 1	186	168	51	7	11	460	203	231	1,317
Injection Water 2	442	262	80	—	—	760	199	682	2,425
Connate Water	68,952	16,736	3,015	386	2,060	146,093	617	100	237,959

Table 3 The basic properties of the core samples used.

Core No.	Length (cm)	Diameter (cm)	Pore Volume (ml)	Gas Permeability (md)	Brine Permeability (md)
26	7.124	3.81	11.32	55.15	~35
27	7.116	3.81	11.98	53.61	~35
55	7.07	3.81	10.34	48.11	~35

viscoelasticity and torque levels as a constant frequency and temperature. The sweeps were conducted over the range of strain, between 0.01% and 100% at a fixed frequency of 1 Hz. The storage modulus and loss modulus were measured as a function of strain.

After the viscoelastic region was fixed, the frequency sweep test was performed to measure the dynamic properties of the fluid sample such as the storage modulus and loss modulus in the specified range of oscillatory frequencies. The measurement was conducted over the range of frequencies between 0.1 rad/s and 100 rad/s at a fixed strain level of 0.25%.

PPG Blocking Test

PPG blocking tests evaluated the blocking capacity of the PPG pack to the open fracture by the coreflooding method. The procedures were:

1. Prepare the PPG samples in injection water 2, and allow to fully swell overnight.
2. Cut the cylindrical limestone core sample longitudinally along the axis, and saturate the two halves with brine.
3. Place the quantitative swollen PPG — without free water — on the cutting section of the core halves. Reassemble the two halves with proper proppant to create an artificial fracture filling with PPG.
4. Pack the core with Teflon and load into a core holder.
5. Inject brine into the core at a flow rate of 0.5 ml/min, 1 ml/min, 2 ml/min, and 4 ml/min, at a confining pressure of 200 psi at ambient temperature, and record the differential pressure.

Results and Discussions

PPG Bulk Properties

The swelling behavior of the four PPG samples in three oil field brines was tested. The swelling ratio was calculated as the volume ratio before and after swelling. Table 4 lists the results. The swelling ratio of HOP-1 was much higher than that of the other three samples. In injection water 1, the swelling ratio was as high as 22.89, while in connate water, the swelling ratio was 4.09. HOP-4 showed the lowest swelling ratio and salinity dependency among the four samples. With increasing salinity, the swelling ratio of HOP-4 decreased slightly from 3.87 in injection water 1 to 2.28 in connate water. HOP-2 and HOP-3 had median swelling capacity and salinity dependency.

The strength of the swollen particles without free water were tested by a rheometer. A dynamic strain sweep test was first performed to determine the range of linear viscoelasticity. Figure 1 shows the typical strain sweep results for HOP-1 in brine. The storage modulus was linear with oscillation strain in the range from 0.01% to 1% in the log-log plot. The strain lever was selected as 0.25% in the frequency sweep test.

Figures 2 to 5 show the frequency sweep results of PPG swelling in three brines. Because salinities of injection water 1 and injection water 2 were similar, the strength of the four PPG samples in the two brines was close to each other. In the connate water with salinity as high as 237,959 mg/L, the samples showed a much higher strength than in the other two brines.

Figure 6 compares the strength of the four samples in injection water 2. The results agreed well with the swelling ratio trend in Table 6, showing that the strength was in an order of HOP-1 < HOP-2 < HOP-3 < HOP-4. The

Table 4 The swelling capacity of the four PPG samples in different brines.

Brine	Salinity (mg/L)	Swelling Ratio			
		HOP-1	HOP-2	HOP-3	HOP-4
Injection Water 1	1,317	22.89	11.81	5.28	3.87
Injection Water 2	2,425	18.49	10.16	4.47	3.87
Connate Water	237,959	4.09	3.33	2.78	2.28

Fig. 1 *The dynamic strain sweep test for HOP-1 in brine.*

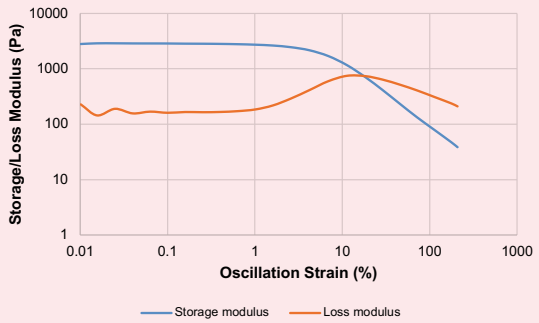

Fig. 2 *The storage modulus of HOP-1 in three brines.*

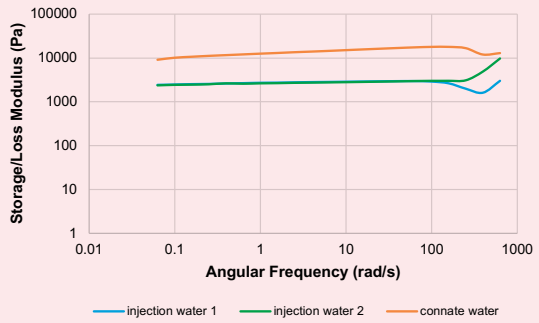

Fig. 3 *The storage modulus of HOP-2 in three brines.*

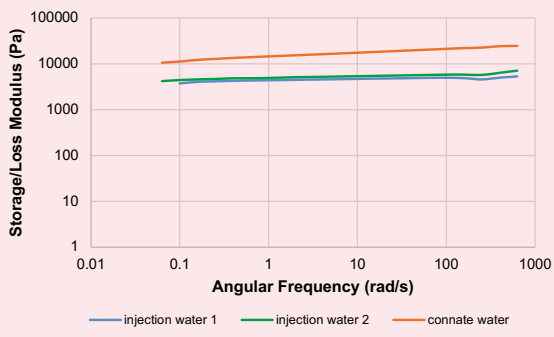

Fig. 4 *The storage modulus of HOP-3 in three brines.*

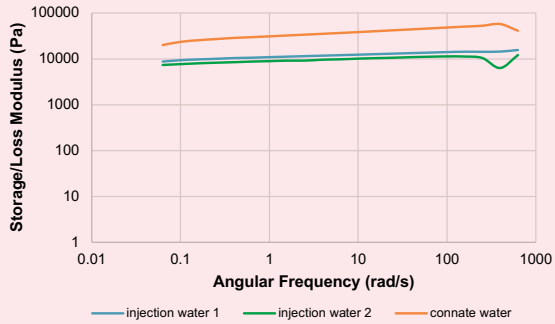

Fig. 5 *The storage modulus of HOP-4 in three brines.*

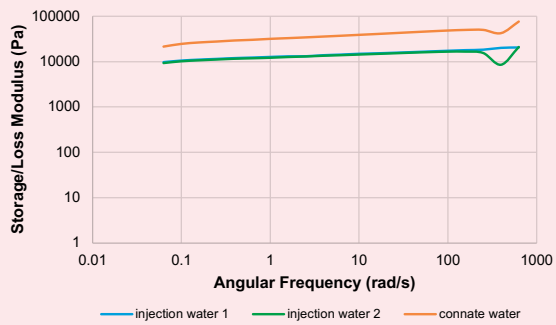

Fig. 6 *The comparison of the four PPG samples in injection water 2.*

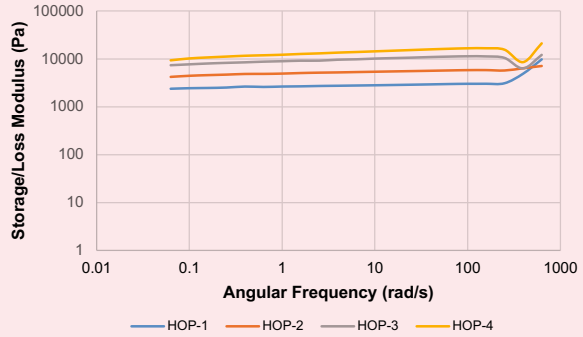

absorbed water weakens the interaction of the macromolecules, resulting in low strength at a high swelling ratio.

PPG Blocking Test

PPG blocking capacities were tested by injecting water into gel packed artificial open fractures. The fractures were made on the cylindrical carbonate outcrop. The core samples were cut longitudinally along the axis to form an open fracture with a length of about 7 cm and width of 3.8 cm. Four small steel slugs were put on the cutting faces as proppant and the fracture heights could be adjusted by the size of the steel proppant. Two fracture heights, 1 mm and 2 mm were used in the tests. The fracture volumes (FV) were 5.4 ml and 2.7 ml, respectively. The water flow through the two kinds of fractures produced very low differential pressure that was hardly detected by the current coreflooding system.

The PPGs were placed manually in the fracture to form a gel pack. The objective here is to evaluate the blocking capacity to water after the gel pack formed in the fracture, and compare the performance of different PPG samples, so the PPG injection and filling processes

were not included. In the application, the PPGs could be packed to different degrees in the fracture based on the injection pressure. Therefore, two types of pack volumes were studied, a loose pack and a firm pack. For the loose pack, about 1 FV of swollen PPGs were placed in the fracture. For the firm pack, the PPG's volume was about 1.5 FV. Table 5 lists the PPG blocking tests that were conducted.

Figures 7 to 16 show the differential pressure change during the water injection into the core plug with the fracture packed with PPG. In all tests, when water was injected, there was water flow in both the core matrix and the gel pack. These flows produced a stable differential pressure along the core plug. The differential pressure increased with the flow rate as long as the gel pack was stable. At a sustained high flow rate, the gel pack could be a breakthrough along with an unstable decreasing pressure. Table 6 summarizes the stable differential pressure in the tests.

With the same PPG sample, the performance was different with the fracture heights and pack volumes. For the blocking test using the same PPG, i.e., HOP-1 (Figs. 7, 8, and 9), HOP-2 (Figs. 10 and 11), HOP-3 (Figs. 12 and 13), and HOP-4 (Figs. 14, 15, and Fig. 16), the PPGs produced higher differential pressure and better blocking to water in a 1 mm fracture than in a 2 mm fracture. With the same fracture height of 2 mm, a firm pack of 1.5 FV produced a much higher differential pressure than the loose pack of 1 FV. These results indicated that PPGs showed better blocking and flow tolerance in the smaller fracture. The degree of PPG packing in the fracture significantly affected the blocking performance. A firm pack could dramatically improve the plugging to the fracture.

Different PPG samples behaved quite differently when

Table 5 *PPG blocking tests in open fracture.*

Test No.	PPG Sample	Particle Size (mm)	Fracture Height (mm)	Particle/Fracture Size Ratio	Pack Volume (FV)
1	HOP-1	2.4	2	1.2	1
2	HOP-1	2.4	1	2.4	1
3	HOP-1	2.4	2	1.2	1.5
4	HOP-2	2.2	2	1.2	1
5	HOP-2	2.2	2	1.2	1.5
6	HOP-3	1.1	2	0.6	1
7	HOP-3	1.1	2	0.6	1.5
8	HOP-4	1.1	2	0.55	1
9	HOP-4	1.1	1	1.1	1
10	HOP-4	1.1	2	0.55	1.5

Fig. 7 *Differential pressure during water injection into HOP-1 packed fracture (1 FV) with height 2 mm.*

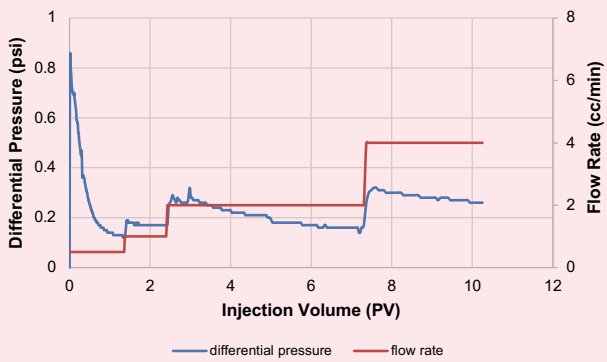

Fig. 8 *Differential pressure during water injection into HOP-1 packed fracture (1 FV) with height 1 mm.*

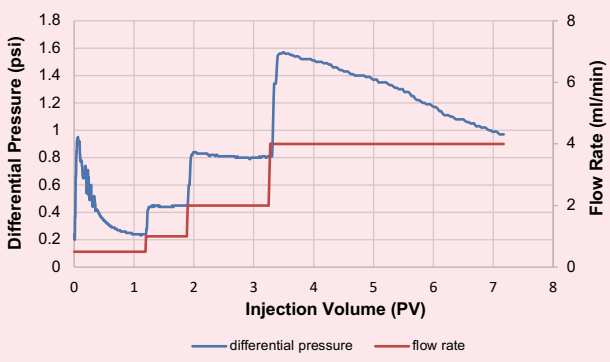

packed in the fracture. For HOP-1 and HOP-2 in the 2 mm and/or 1 mm fracture with 1 FV pack (Figs. 7, 8, and 10), the differential pressure first increased rapidly and then decreased to a stable value at the beginning of water injection. There was no such pressure built-up in the tests using HOP-3 and HOP-4. The stable differential pressure and breakthrough flow rate varied significantly for the four samples.

In the tests using 1 FV packing, HOP-1 produced the lowest differential pressure to water flow among the four

Fig. 9 *Differential pressure during water injection into HOP-1 packed fracture (1.5 FV) with height 2 mm.*

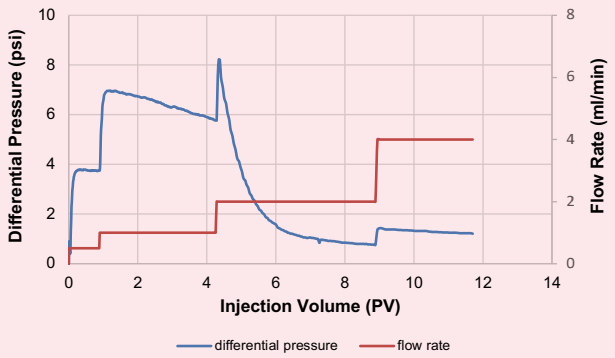

Fig. 10 *Differential pressure during water injection into HOP-2 packed fracture (1 FV) with height 2 mm.*

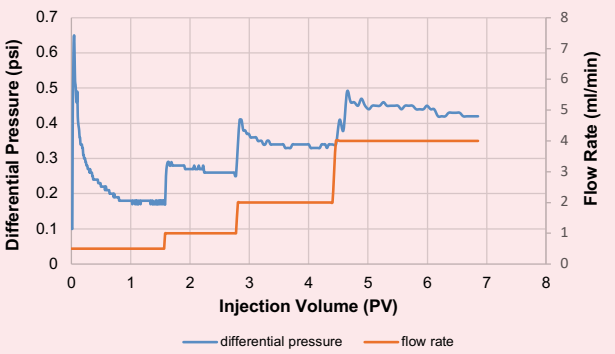

Fig. 11 *Differential pressure during water injection into HOP-2 packed fracture (1.5 FV) with height 2 mm.*

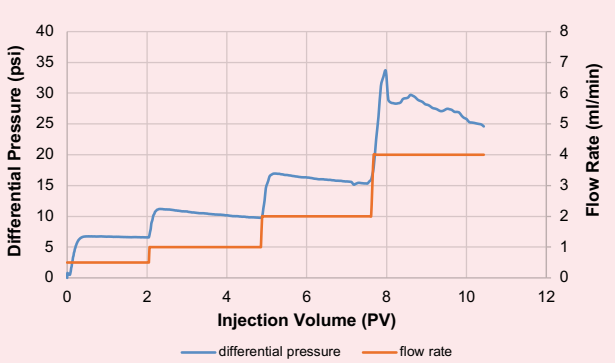

Fig. 12 *Differential pressure during water injection into HOP-3 packed fracture (1 FV) with height 2 mm.*

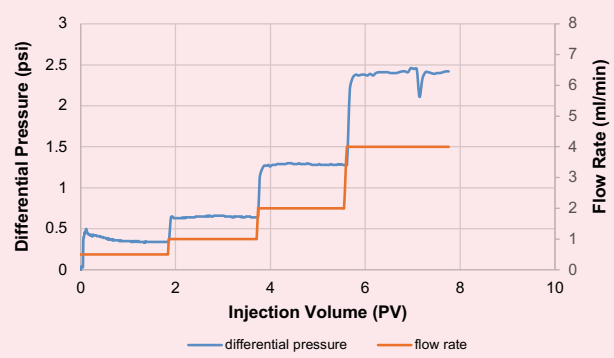

Fig. 13 *Differential pressure during water injection into HOP-3 packed fracture (1.5 FV) with height 2 mm.*

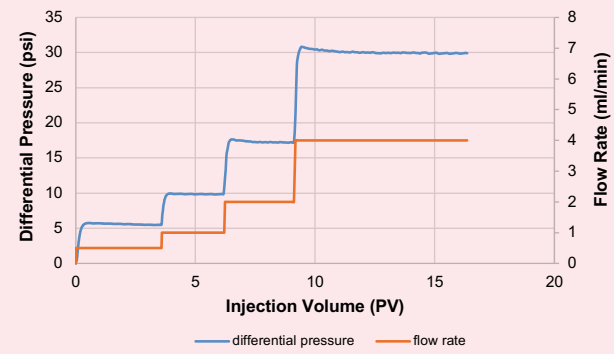

Fig. 14 *Differential pressure during water injection into HOP-4 packed fracture (1 FV) with height 2 mm.*

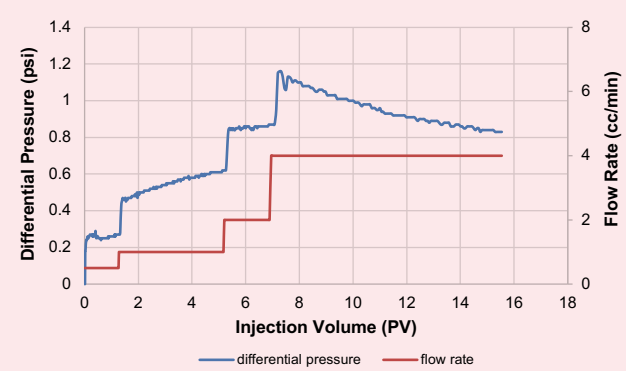

Fig. 15 *Differential pressure during water injection into HOP-4 packed fracture (1 FV) with height 1 mm.*

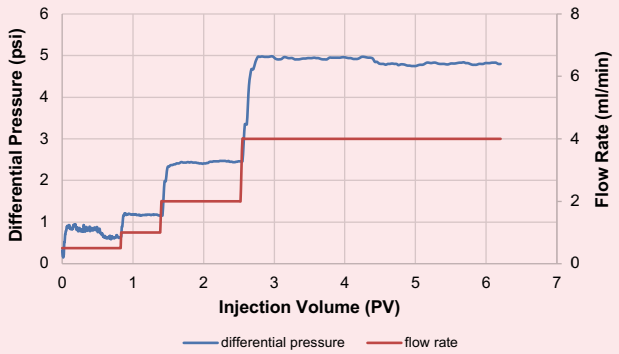

Fig. 16 *Differential pressure during water injection into HOP-4 packed fracture (1.5 FV) with height 2 mm.*

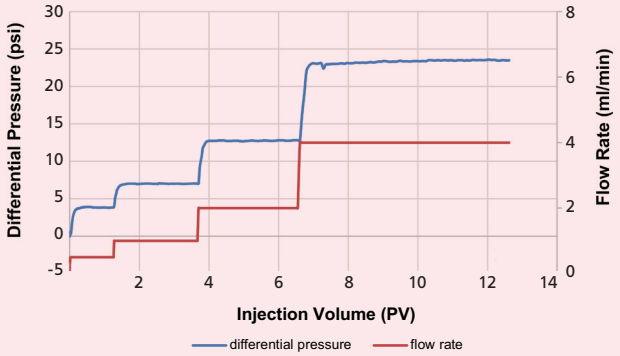

Table 6 *The stable differential pressure (psi) in the PPG blocking tests using 1 mm and 2 mm fractures.*

Flow Rate (ml/min)	HOP-1			HOP-2		HOP-3		HOP-4		
	1 mm Fracture	2 mm Fracture	2 mm Fracture	2 mm Fracture	2 mm Fracture	2 mm Fracture	2 mm Fracture	1 mm Fracture	2 mm Fracture	2 mm Fracture
	1 FV Pack	1 FV Pack	1.5 FV Pack	1 FV Pack	1.5 FV Pack	1 FV Pack	1.5 FV Pack	1 FV Pack	1 FV Pack	1.5 FV Pack
0.5	0.24	0.12	3.75	0.17	6.61	0.34	5.48	0.64	0.27	3.81
1	0.45	0.17	—	0.26	9.84	0.65	9.80	1.16	0.61	6.97
2	0.81	—	—	0.33	15.41	1.28	17.21	2.45	0.86	12.78
4	—	—	—	0.42	—	2.41	29.87	4.82	—	23.51

PPG samples. The breakthrough flow rate was 2 ml/min in fractures of 2 mm. HOP-2 had a slightly high differential pressure and the gel pack was not broken through at a flow rate as high as 4 ml/min. HOP-3 produced the highest differential pressure among the four samples, and the gel pack was flow resistant. Although the strength was higher, the differential pressure caused by the HOP-4 pack was slightly lower than that caused by HOP-3. The gel pack was broken through at a flow rate of 4 ml/min.

The differences may be explained by the strength nature of the four PPGs. The strength or elastic modulus of HOP-1, HOP-2, HOP-3, and HOP-4, was 2,800 Pa, 5,300 Pa, 9,700 Pa, and 13,800 Pa, respectively. When packed in the fracture, samples with a low strength are much deformable and form a close packing between the particles with very little pores. The injected water cannot penetrate easily in the pack at the very beginning, which results in a pressure buildup. At the same time, the particles deform with the pressure and a connected flow channel forms along the deformed particles.

After water breaks through the PPG pack, the pressure decreases to become stable. When the flow rate is high enough, the water flow moves the particles. The differential pressure keeps decreasing with the movement. On the contrary, when the samples with high strength are packed in the fracture, it is much more permeable, due to the interparticle pores.

The pressure of the water injection is stable with no abrupt pressure buildup. At a high flow rate, the gel particles are more likely to move with water because of the lack of deformation. Therefore, the pack has the risk to be flushed away in the fracture. Proper deformation seems to help the particles withstand the water flush and avoid lasting movement. This may be the reason that the HOP-3 pack with a lower strength showed higher pressure buildup and flow resistance than the HOP-4 pack.

On one hand, the deformable PPG produces a firm pack with few interparticle pores, which can block the fracture efficiently. On the other hand, the deformation

enables the PPG pack to easily break through by the flow pressure, and therefore, the flow tolerance was not good. The median strength balanced the blocking and flow tolerance, resulting in a better pressure buildup.

Conclusions

This work studied the PPG blocking behavior by a series of coreflooding tests in open fractured carbonate cores. The effects of the PPG strengths, pack density, and particle/fracture size ratio were also investigated.

1. The swelling capacities of the PPG showed a reverse correlation with brine salinity. The swelling ratio of HOP-1, HOP-2, HOP-3, and HOP-4 decreased in order.
2. The storage modulus of the four PPG samples increased from a magnitude of 2,000 Pa to 14,000 Pa, and the average particle size decreased from 2.4 mm to 1.1 mm.
3. The PPG samples presented better blocking performance in smaller fracture cores. A firm pack could significantly improve the blocking performance in the open fracture.
4. The strength of the PPG samples affected the PPG blocking performance significantly. The HOP-3 pack showed better performance in open fractures than the other samples, due to the well-adjusted properties in blocking and flow tolerance.

References

1. Breston, J.N.: "Selective Plugging of Waterflood Input Wells Theory, Methods, and Results," *SPE Journal of Petroleum Technology*, Vol. 9, Issue 3, March 1957, pp. 26-31.
2. Sydansk, R.D. and Moore, P.E.: "Gel Conformance Treatments Increase Oil Production in Wyoming," *Oil & Gas Journal*, January 1992, pp. 40-45.
3. Serignt, R.S. and Liang, J.: "A Survey of Field Applications of Gel Treatments for Water Shutoff," SPE paper 26991, presented at the SPE Latin America/Caribbean Petroleum Engineering Conference, Buenos Aires, Argentina, April 27-29, 1994.
4. Bai, B., Li, L., Liu, Y., Wang, Z., et al.: "Preformed Particle Gel for Conformance Control: Factors Affecting its Properties and Applications," SPE paper 89389, presented at the SPE/DOE Symposium on Improved Oil Recovery, Tulsa, Oklahoma, April 17-21, 2004.
5. Sydansk, R.D., Xiong, Y., Al-Dhafeeri, A.M., Schrader, R.J., et al.: "Characterization of Partially Formed Polymer Gels for Application to Fractured Production Wells for Water Shutoff Purposes," SPE paper 89401, presented at the SPE/DOE Symposium on Improved Oil Recovery, Tulsa, Oklahoma, April 17-21, 2004.
6. Coste, J-P., Liu, Y., Bai, B., Li, Y., et al.: "In-Depth Fluid Diversion by Pre-Gelled Particles. Laboratory Study and Pilot Testing," SPE paper 59362, presented at the SPE/DOE Improved Oil Recovery Symposium, Tulsa, Oklahoma, April 3-5, 2000.
7. Han, M., Alshehri, A.J., Krinis, D. and Lyngra, S.: "State-of-the-Art of In-Depth Fluid Diversion Technology: Enhancing Reservoir Oil Recovery by Gel Treatments," SPE paper 172186, presented at the SPE Saudi Arabia Section Technical Symposium and Exhibition, April 21-24, 2014.
8. Bai, B., Zhou, J. and Yin, M.: "A Comprehensive Review of Polyacrylamide Polymer Gels for Conformance Control," *Petroleum Exploration and Development*, Vol. 42, Issue 4, August 2015, pp. 525-532.
9. Bai, B., Liu, Y., Coste, J-P. and Li, L.: "Preformed Particle Gel for Conformance Control: Transport Mechanism through Porous Media," *SPE Reservoir Evaluation and Engineering*, Vol. 10, Issue 2, April 2007, pp. 176-184.
10. Zhang, H. and Bai, B.: "Preformed Particle Gel Transport through Open Fractures and Its Effect on Water Flow," *SPE Journal*, Vol. 16, Issue 2, June 2011, pp. 388-400.
11. Imqam, A., Bai, B., Al Ramadan, M., Wei, M., et al.: "Preformed Particle Gel Extrusion through Open Conduits during Conformance Control Treatments," *SPE Journal*, Vol. 20, Issue 5, October 2015, pp. 1083-1093.
12. Imqam, A., Bai, B. and Delshad, M.: "Preformed Particle Gel Propagation through Super-K Permeability Sand and Its Resistance to Water Flow during Conformance Control," SPE paper 176429, presented at the SPE/IATMI Asia Pacific Oil and Gas Conference and Exhibition, Nusa Dua, Bali, Indonesia, October 20-22, 2015.
13. Imqam, A., Wang, Z., Bai, B. and Delshad, M.: "Effect of Heterogeneity on Propagation, Placement, and Conformance Control of Preformed Particle Gel Treatment in Fractures," SPE paper 179705, presented at the SPE Improved Oil Recovery Conference, Tulsa, Oklahoma, April 11-13, 2016.
14. Imqam, A., Wang, Z. and Bai, B.: "Preformed Particle Gel Transport through Heterogeneous Void Space Conduits," *SPE Journal*, Vol. 22, Issue 5, October 2017, pp. 1437-1447.
15. Wang, Z. and Bai, B.: "Preformed Particle Gel Placement and Plugging Performance in Fractures with Tips," *SPE Journal*, Vol. 23, Issue 6, December 2018, pp. 2316-2326.
16. Wu, D., Zhou, K., An, Z. and Hou, J.: "Experimental Study on the Matching Relationship between PPG Size and Reservoir Heterogeneity," SPE paper 193709, presented at the SPE International Heavy Oil Conference and Exhibition, Kuwait City, Kuwait, December 10-12, 2018.

About the Authors

Dongqing Cao

M.S. in Petroleum Engineering, China University of Petroleum

Dongqing Cao joined the Aramco Beijing Research Center in July 2012 as a Petroleum Engineer. His research areas include physical modeling by coreflooding and micromodel, oil field chemicals for oil production, fluid diversion, and conformance control.

Dongqing has authored and coauthored 14 conference papers and journal papers, and published two patents.

He received both his B.S. and M.S. degrees in Petroleum Engineering from the China University of Petroleum, Qingdao, China.

Dr. Ayman M. Al-Mohsin

Ph.D. in Petroleum Engineering, Missouri University of Science and Technology

Dr. Ayman M. Al-Mohsin joined Saudi Aramco in 2014 as a Research Engineer. He is currently a Petroleum Engineer working in Smart Fluid Focus Area in the Production Technology Division of Saudi Aramco's Exploration and Petroleum Engineering Center – Advanced Research Center (EXPEC ARC). Ayman's research interests include water and gas shutoff using chemical means.

He received his B.S. degree in Mechanical Engineering from the University of New Haven, West Haven, CT; his M.S. degree in Petroleum Engineering from New Mexico Tech, Socorro, NM; and his Ph.D. degree in Petroleum Engineering from Missouri University of Science and Technology, Rolla, MO.

Dr. Ming Han

Ph.D. in Chemistry, University of Rouen

Dr. Ming Han is a Petroleum Engineering Consultant in chemical enhanced oil recovery, working in Saudi Aramco's Exploration and Petroleum Engineering Center – Advanced Research Center (EXPEC ARC). Before joining Saudi Aramco in 2007, he worked for the China National Offshore Oil Corporation (CNOOC), where he was Lead Engineer in Oil Field Chemistry at the CNOOC Research Center working to implement an offshore polymer flooding project.

For more than 10 years of his career, Ming worked for the Research Institute of Petroleum Exploration and Development (RIPED) in China as a Research Engineer, conducting laboratory studies and field pilots in water shutoff, profile modification, polymer and chemical flooding. He also worked at Hycal Energy Research in Canada as a Research Engineer.

Ming has authored or coauthored more than 60 technical papers and holds more than 10 granted patents and four industrial standards. He has also served as a technical editor for many international journals in the industry. In 1982, Ming received his B.S. degree in Polymer Chemistry from Jilin University, Changchun, China. He received his M.S. degree from the University of Paris VI, Paris, France, and his Ph.D. degree from the University of Rouen, Mont-Saint-Aignan, France, both in Polymer Physico-Chemistry.

Ming is a member of the Society of Petroleum Engineers (SPE) and the American Chemical Society (ACS).

Dr. Bader G. Alharbi

Ph.D. in Petroleum Engineering, Heriot-Watt University

Dr. Bader G. Alharbi joined Saudi Aramco in 2006 as a Petroleum Engineer. Bader is currently working in the Production Technology Division of Saudi Aramco's Exploration and Petroleum Engineering Center – Advanced Research Center (EXPEC ARC), where he is a focus area champion of smart fluid. Bader's research interests include well stimulation and scale mitigation.

He has authored and coauthored more than 21 technical papers. Bader has two granted patents and more than 10 submitted invention disclosures.

He received his B.S. degree in Chemical Engineering, and his M.S. degree in Petroleum Engineering, both from King Fahd University of Petroleum and Minerals (KFUPM), Dhahran, Saudi Arabia. Bader received his Ph.D. degree in Petroleum Engineering from Heriot-Watt University, Edinburgh, Scotland, U.K.

Enhanced Regained Permeability and Fluid Flow Back from Tight Sandstone and Carbonate Oil Reservoirs with Unique Flow Back Chemistry

Dr. Rajesh K. Saini, Brady Crane, Nicole R. Shimek, Dr. Weiran Wang and Brent Cooper

Abstract /

Large amounts of aqueous-based fluids used in hydraulic fracturing of tight formations is not fully recovered immediately after the treatment, resulting in increased water saturation, water blockage, clay swelling, reduced relative permeability, and long-lasting formation damage that impedes production. To enhance flow back fluid recovery, nanoemulsion-based flow back aids were developed for oil-bearing sandstone and carbonate formations.

The flow back aids were formulated using a blend of high temperature stable ester-based solvents, alcohols, and surfactants to form optically clear nanoemulsions. The flow back aids were characterized by measuring the emulsion particle size, surface tension, and interfacial tension (IFT). The performance of the flow back aids were tested using sand and carbonate particle packed columns to determine adsorption tendencies of the surfactants and the displacement efficiency of aqueous fracturing fluid by crude oil.

Emulsion tests were conducted to determine emulsion breaking efficiency of the flow back aids between aqueous fracking fluid and crude oil. Finally, core flow tests were performed with low permeability cores (1 md to 15 md) at reservoir conditions to determine the regained permeability in the presence of flow back aids. All the developed flow back aids demonstrated low surface tension (22 mN/m to 30 mN/m) and IFT (< 6 mN/m), which is necessary for reducing capillary pressure.

The particle size of the nanoemulsions was found to be 5 nm to 15 nm. The flow back aids were able to prevent the formation of the emulsion with crude oil. It has been found that nanoemulsions formulated using nonionic and anionic surfactants worked better for sandstone, whereas nonionic and cationic surfactant-based formulations worked better for carbonate. These formulations not only provide quick aqueous fluid displacement, but also greatly enhance the rate of oil flow in core flow experiments conducted with broken slick water fracturing fluids. It was determined that in the absence of a flow back aid, the regained permeability was around 40%, whereas with flow back aids it was increased to 65% to 75%.

This article demonstrates the effectiveness of flow back enhancers to quickly recover the injected aqueous fracturing fluid, thereby reducing water saturation, which in turn enhances productivity, and shows the benefit of applying the chemistry for low permeability oil reservoirs.

Introduction

Aqueous-based fluids are preferred for hydraulic fracturing treatments due to their low cost and ease of handling. The retention of injected aqueous fluid can negatively affect the production of hydrocarbons. Therefore, different chemical additives and surfactants have been investigated to increase the recovery of fracturing fluids[1, 2]. In unconventional wells (shale, sandstone, and carbonate containing oil and gas wells) with low permeability (< 1.0 md) it has been shown that water-based fluids can significantly reduce reservoir permeability, and impair well productivity[3, 4]. Some of the causes of impaired productivity include increased water saturation near the wellbore, clay swelling, and increased ductility of formation and proppant embedment.

During hydraulic fracturing of tight formations, spontaneous imbibition occurs within low permeability in undersaturated reservoirs. The aqueous fluid then gets trapped in pore spaces as well as within the created microfractures and induced fractures[5]. During the production phase, when oil and gas flows through this low permeability zone, it may take a considerably long time before the invaded fluid is expelled[6]. The depth of imbibition into the rock is determined not only by permeability and saturation of the reservoir, but also by the chemical affinities between the oil/gas, rock reservoir fluid, and the invading fluids.

To remove the aqueous fracturing fluid fluids from the formation, the capillary pressure needs to be significantly reduced to produce the imbibed fluid. Capillary pressure in porous media is usually simplified in the form of the following equation, Eqn. 1:

$$P_c = v.\ Cos\ \theta/d \quad (1)$$

where, γ = surface tension (mN/m or Dyne/cm), *Cos* θ = cosine of contact angle between the rock, fluid and gas,

d = diameter of pores (mm), and P_c = capillary pressure (Pascal).

To remove the aqueous fluid from the porous channel, the capillary pressure needs to be overcome, which can be done by either reducing surface tension or increasing the contact angle. Surface active materials have been used to reduce surface tension and recently emulsion-based flow back enhancers are being used to recover the invaded fracturing fluid from tight formations.

Flow back aids or flow back enhancers are usually mixtures or emulsions of various kinds of surfactants, solvents, or both. They are added to stimulation treatment fluids to reduce capillary pressure by reducing interfacial tension (IFT) and surface tension. The stimulation of unconventional wells needs around 37,854 m^3 to 75,708 m^3 (10 to 20 million gallons) of slick water fluid per well[7-10]. The amount of flow back enhancer used in these fluids range from 0.1% v/v to 0.2% v/v, which can substantially increase the cost of the treatment.

During the past decade, microemulsions and/or nanoemulsions have gained more interest in hydraulic fracturing. It has been demonstrated that wells treated with fluids containing microemulsions and/or nanoemulsion flow back enhancer additives were more productive than a well that was treated with traditional surfactants. Enhancing the penetration and cleanup of water-based fracture fluids and allowing higher fluid return and hydrocarbon production are among common attributes to such additives.

Based on the superiority of microemulsion and nanoemulsion-based fluids over traditional surfactant fluids in flow back enhancement, we focused our development on the formulation of nanoemulsion-based flow back enhancers[11-14]. These fluids are specifically designed for carbonate and sandstone formations containing oil, as you need different formulations for different mineralogy of formation and also with formation containing oil and gas. Flow back enhancers do not work for all formations due to the interactions between the surfactant, the formation mineralogy and oil that dictate the effectiveness of the fluid.

Materials and Methods

Materials

All the chemicals used to formulate the flow back enhancer were of analytical grade and used as received without any further purification. Deionized (DI) water was used in the formulation. Isopropanol, propylene glycol, triethylene glycol, and potassium chloride (KCl) were obtained from VWR Scientific. Secondary alcohol ethoxylate and Dowanol™ DPM glycol ether were obtained from Dow Chemicals. Pluronic L64 (Mn ~2900) was obtained from BASF, and castor oil, ethoxylate, was obtained from Vantage. Dodecylbenzene sulfonic acid was attained from TCI America, modified quaternary imidazoline from Lubrizol, and an unsaturated ester solvent from Elevance Renewable Sciences. SafeCarb 250 (250 to 300 micron carbonate particles) was obtained from Newpark, and 80 to 100 mesh sand particles from Carbo Ceramics.

A friction reducer polymer (partially hydrolyzed polyacrylamide Mw > 9 million) was prepared in-house. Berea sandstone and Austin chalk carbonate cores were procured from Kocurek Industries.

Preparation of Flow Back Enhancer Formulations

Three nanoemulsion-based flow back enhancers, namely FBE-A, FBE-B, and FBE-C were formulated by blending different surfactants, solvents, alcohols, and water, Table 1. The concentration of surfactants and solvents in the nanoemulsion are also provided. The sequence of the addition of the chemicals are in the order of: water, alcohol, surfactant, and solvent.

All the chemicals were mixed for 30 minutes and when everything was dissolved an unsaturated ester solvent from Elevance was added at the end and mixed additionally for 10 minutes. It was noted that an initial milky solution was formed but on further mixing it turned to a clear solution without any layer or separation. The

Table 1 *Formulation of flow back enhancers FBE-A, FBE-B, and FBE-C.*

Flow Back Enhancer	Surfactant/Solvent Blend	Activity (%)	Nanoemulsion Charge
FBE-A	DI water, mixture of alcohols, unsaturated ester solvent	65	Nonionic
	Secondary alcohol ethoxylate, pluronic L64, castor oil ethoxylate	35	
FBE-B	DI water, mixture of alcohols, unsaturated ester solvent	65	Cationic
	Secondary alcohol ethoxylate, castor oil ethoxylate, modified quaternary imidazoline	35	
FBE-C	DI water, mixture of alcohols, unsaturated ester solvent	65	Anionic
	Secondary alcohol ethoxylate, castor oil ethoxylate, pluronic L64, dodecylbenzene sulfonic acid	35	

Elevance unsaturated ester was used as an oil phase for the nanoemulsion formation.

Emulsion Particle Size Determination

The particle size of the flow back enhancer nanoemulsions were measured by a Malvern Zetasizer. This measurement was done directly on the flow back additive as well as by adding a flow back enhancer (0.1% v/v to 0.2% v/v concentration) to a 6% KCl solution in water.

General Procedure for the Preparation of Fluids

Preparation of 6% KCl containing flow back enhancer: To 250 ml of water in a beaker, 15 g of KCl was added and stirred to get a clear solution. To 100 ml of this solution, 0.2 ml of flow back enhancer was added and mixed for 5 minutes. This diluted fluid was used for the gravity drainage fluid recovery column test and other tests.

Preparation of slick water fluid for core flow and emulsion test: To 250 ml of water in a Waring blender, 15 g of KCl and 0.5 ml of flow back enhancer (0.2% v/v) were added and mixed for 5 minutes. To this stirred solution, 0.5 ml (0.2% v/v) of the friction reducer was added and mixed for another 10 minutes to hydrate the polymer. Then, 0.06 g (0.024 wt%) of sodium persulfate was added and the solution was placed in a heated water bath at 180 °F for 12 hours. This broken fluid was used to run the core flow and emulsion tests.

Surface tension and IFT measurement: The surface tension measurement was done on a Rame-Hart Model 210 Goniometer/Tensiometer. The instrument permits the measurement of both surface tension as well as IFT on pendant and sessile drop. The 6% KCl fluid solution containing 0.1% v/v to 0.2% v/v of flow back enhancer was used to measure the surface tension and IFT. For reference, water and a 6% KCl solution was also included in the testing. Measurements were done in triplicate and the average reported for each surface tension.

The oil/water IFT was measured using an SVT 20 N spinning drop video tensiometer from DataPhysics Instruments. The IFT was calculated using the following equation (Vonnegut evaluation). The IFT was determined according to a single measurement method, Eqn. 2:

$$\sigma = \frac{(\rho_w - \rho_o)\cdot R^3 \cdot \omega^2}{4} \qquad 2$$

where, σ = the oil/water IFT (mN/m), p_w = density of water (1.0 g/mL), p_o = density of crude oil (0.8378 g/mL), w = rotational speed (rpm) and R = width of the oil droplet (mm). The density of crude oil (p = 0.8378 g/mL) was measured by using a densitometer.

Contact Angle Measurement

Contact angle measurement on flame cleaned glass slide: Glass slides were flame cleaned by holding it with tweezers in a Bunsen burner flame. The glass slide was then air cooled. A drop of fluid with a 0.2% v/v flow back enhancer was then placed on the glass slide and the contact angle was measured using a pendant drop tensiometer.

Contact angle measurement on flame cleaned glass slide followed by flow back fluid: A glass slide was flame cleaned by holding it with tweezers in a Bunsen burner flame and then air cooled. The slide was then dipped in a 0.2% v/v flow back enhancer solution in 6% KCl for about 10 minutes and then dried in an oven (80 °C for 30 minutes). A drop of DI water was placed on the pretreated slide and the contact angle was measured — it measures the ability of the flow back additive to alter the contact angle of the surface.

Emulsion Break Test

Emulsion break tests were performed in a 15 mL polypropylene conical tube. In the blank test, 5 ml of broken slick water fracture fluid without any flow back enhancer and 5 ml of crude oil were added to the conical tube and capped. The tube was shaken vigorously by hand for 20 to 25 seconds to form an emulsion. The tube was then placed without disturbing to demulsify at room temperature for 15 minutes and then in a water bath maintained at 65.56 °C (150 °F) for 40 minutes. The conical tube was taken out of the water periodically to take pictures to assess the emulsion breakage.

To test the flow back enhancer, an aqueous broken slick water fracturing fluid containing 0.2% v/v of flow back enhancer was used. Crude oil was added to 5 ml of this solution containing 0.2% v/v flow back enhancer in the conical tube 5 ml. The procedure mentioned above was followed and emulsion breakage pictures taken.

Gravity Drainage Fluid Recovery Column Test

Step 1: Packing the column and finding the pore volume (PV): Figure 1 depicts the experimental setup for this test. An 8.5-cm long, 1.6-cm internal diameter short glass column equipped with stainless screen of 200 mesh and a drainage valve with a stopcock was used for this test. The valve was closed before the column was packed. The column was gravity packed by pouring

Fig. 1 The gravity drainage fluid recovery column apparatus used.

approximately 10 mL of 6% KCl (or 10 mL of 6% KCl in water containing 0.2% v/v of flow back enhancer) into the column followed by a slow, continuous addition of 10 g of 40/70 mesh sand while vibrating the column.

The column was kept vibrating until the pack height in the column had stabilized. The excess fluid above the pack was removed from the column so that the level of the liquid exactly matched the level of the sand in the column. The PV of the packed column was calculated as the difference in volume of fluid prior to the column packing and after the column has been packed.

Step 2: Treatment of pack with flow back fluid followed by oil drainage: Three additional PVs of 6% KCl or 6% KCl containing 0.2% v/v of flow back enhancer was passed through the column by opening the valve and draining fluid through the pack, while constantly replenishing the fluid on the top of the pack to prevent drying of the column. The drained fluid was collected in a graduated cylinder. After the last PV was passed through the column, the level of the fluid was adjusted exactly to the level of the sand bed by closing the valve once the fluid had become level.

Crude oil was then added to the top of the sand pack to form a 5 cm oil column above the bed. The valve was then opened, and the displacement weight of aqueous fluid was collected in a graduated cylinder. This cylinder was kept on a balance connected to a data logger, which automatically collects weight with respect to time.

The oil height above the sand bed was kept constant at 5 cm by adding of more crude oil by using a dropper. The experiment was conducted for 30 to 60 minutes depending on the flow rate. When both brine and oil were produced from the column, they were separated and weighed separately. The cumulative fraction weights were divided by PV weight and reported as a percentage of fluid recovery with time. The breakthrough of oil with time was also noted.

Amott Cell Imbibition Test

Amott cells were used for spontaneous imbibition testing, specifically to compare the release of oil from the sand core when exposed to a variety of blends of 6% KCl and 0.2% v/v concentration of flow back enhancers. Berea sandstone or Austin chalk core plugs with an approximate permeability of 1 md to 5 md were utilized for testing. The clean dry cores were saturated under vacuum with kerosene oil. The mass/volume of oil uptake was determined gravimetrically.

The saturated core plugs were then placed in an Amott cell containing various treatment solutions made up of 6% KCl brine and a flow back concentration of 0.2% v/v. The released kerosene was then recorded as a cumulative volume over time and normalized to the volume of oil that was initially imbibed into the core. The testing was conducted at room temperature and the kerosene released was monitored for a period of 24 hours.

Figure 2 is a schematic of the setup of the Amott cell apparatus.

Core Flow Regained Permeability Test

Core flow tests were performed in a coreflood apparatus using Berea gray sandstone cores of 15.24 cm (6") length and 3.81 cm (1.5") diameter. The average initial permeability (kerosene) of the cores used for the tests ranged between 5 md to 15 md. A confining pressure of 13.79 MPa (2,000 psi) and back pressure of 6.89 MPa (1,000 psi) was applied to the core. The core holder was heated to a temperature of 93.33 °C (200 °F).

Fig. 2 *A schematic of the Amott cell imbibition apparatus.*

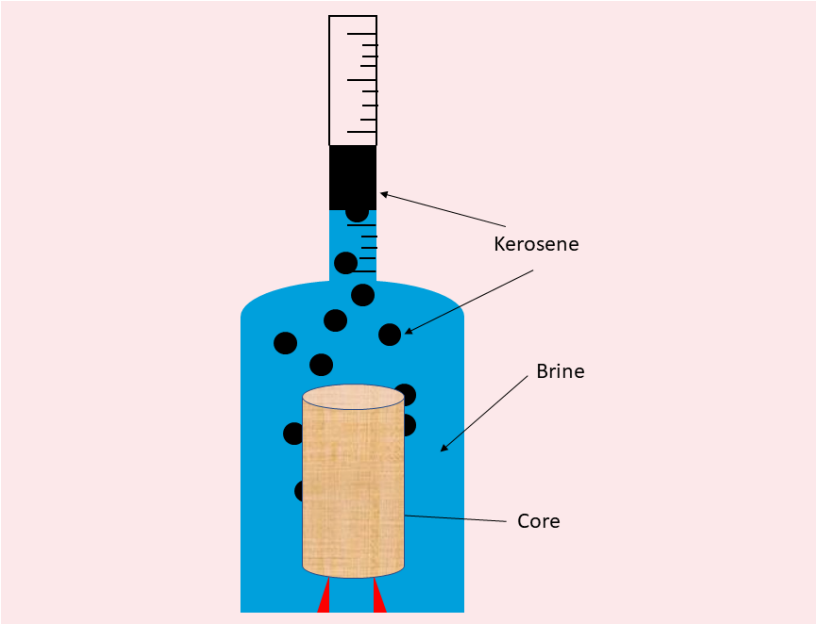

The core was saturated under pressure and temperature by flowing kerosene through the core at the rate of 5 mL/min in the production direction until a stable reading was obtained. The initial permeability was calculated from this stable reading. After a stable reading — variation of less than 2.5% was observed over 5 PVs during injection — was obtained, broken fracture fluid in 6% KCl containing 0.2% v/v of flow back enhancer was pumped in the opposite direction at 5 mL/min for 12 minutes, to simulate the same flow and a treatment volume of approximately 2 PVs. The core was shut-in overnight (16 hours) at temperature and then kerosene was injected in the production direction at 5 mL/min until a stable reading was obtained. The stable reading gives the final permeability. From initial and final permeability, the percentage of regained permeability was calculated. The core flow apparatus schematic is given in Fig. 3.

Results and Discussions

Three new flow back enhancer formulations, FBE-A, FBE-B, and FBE-C, were developed for use in hydraulic fracturing applications of carbonate and sandstone reservoirs containing oil. In this study the performance of the newly developed flow back enhancers were evaluated.

Flow Back Enhancer Formulations

The new formulations were prepared by blending various surfactants, alcohols, and solvents in the form of an

Fig. 3 *Core flow apparatus setup.*

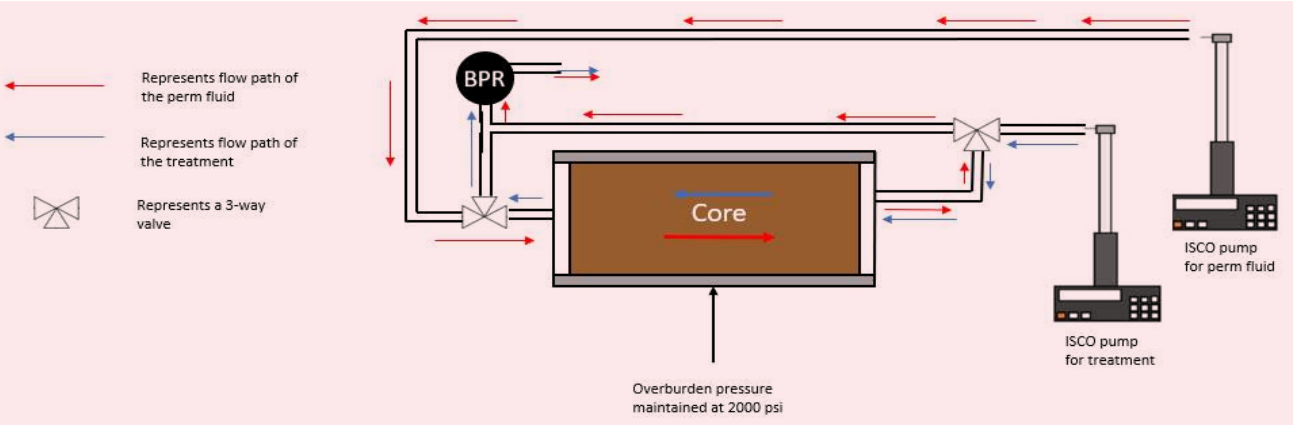

aqueous mixture to form oil-in-water nanoemulsions. The FBE-A flow back enhancer was designed to be nonionic in character, the FBE-B as cationic in character, and the FBE-C as anionic in character.

Table 2 lists the formulation of the three developed flow back enhancers. The different materials in the formulation were previously listed in Table 1. The oil phase (unsaturated ester solvent) was added at the end after solubilizing the other components. All of the formulations were prepared at an active surfactant concentration of 35 wt%. A concentration of 0.2% v/v flow back enhancer was used in the treatment fluid unless mentioned otherwise. All of the flow back enhancers were designed in such a way to achieve low surface tension and IFT, good demulsification properties, low adsorption on the formation's mineral surface, and to provide performance for quick fluid recovery.

The flow back enhancer formulations contain a demulsifier with a hydrophilic-lipophilic balance (HLB) in the range of 10 to 16, nonionic surfactants for low adsorption, different mixtures of solvent to cover wide areas of the Hansen solubility chart, and a solvent phase that has a higher flash point than typical flow back enhancers. For the sandstone formations, an anionic surfactant was used as a combination of flow back enhancer in one of the formulations because silica has a negative charge, and therefore, the anionic surfactants will not adsorb onto it, but at the same time will provide low surface tension and IFT.

Sulfonate-based surfactants are good surfactants as they have high temperature stability and are compatible with divalent ions in water. For carbonate formations, which have a slightly positive charge, a cationic surfactant was included in one of the flow back enhancers, as both positive charges will repel each other, thereby lowering the adsorption.

Surface Tension, IFT and Emulsion Droplet Size

Table 3 shows that all the flow back additives developed have a surface tension of less than 31 mN/m at a concentration of 0.2% v/v. We have also measured the surface tension of water and 6% KCl as standard for comparison purposes. In comparison to water, the surface tension of the solution containing 0.1% and 0.2% v/v of FBE in 6% KCl was much lower in comparison to water and 6% KCl solution. The low value of surface tension lowers the capillary pressure in the tight formation that enhances the production of flow back fluid and oil.

IFT was measured with a spinning drop tensiometer using crude oil and flow back enhancer at 0.1% v/v to 0.2% v/v in 6% KCl. As seen in Table 3, water and 6% KCl have an IFT of 28.85 mN/m and 24.48 mN/m when measured with crude oil, respectively. When a 0.1% v/v to 0.2% v/v flow back enhancer was used with the 6% KCl, the IFT dropped significantly. A lower IFT helps in the prevention of water and oil blocks in the formation, and helps in enhanced fluid recovery.

The particle size of the flow back enhancer emulsion

Table 2 *The flow back enhancer formulations.*

Flow Back Enhancer	Charge	Surfactant Activity (wt%)	Remarks	Solvent Used
FBE-A	Nonionic	35%	Nanoemulsion	Ester with high Fp
FBE-B	Cationic	35%	Nanoemulsion	Ester with high Fp
FBE-C	Anionic	35%	Nanoemulsion	Ester with high Fp

Table 3 *Surface tension, IFT, and the size of the emulsion droplets of FBE in various types of fluids.*

Fluids	Charge	FBE Concentration	Surface Tension (mN/m)	Interfacial Tension with Crude Oil (mN/m)	Emulsion Droplet Size (nm)
Water	Neutral	0	71.26	28.85	—
6% KCl	Neutral	0	73.74	24.48	—
Crude oil	—	0	38.75	—	—
FBE-A	Nonionic Nanoemulsion	0.1% v/v in 6% KCl	30.80	5.16	5.0
FBE-A	Nonionic Nanoemulsion	0.2% v/v in 6% KCl	30.69	5.80	5.5
FBE-B	Cationic Nanoemulsion	0.1% v/v in 6% KCl	23.3	0.618	6.0
FBE-B	Cationic Nanoemulsion	0.2% v/v in 6% KCl	21.34	0.616	8.0
FBE-C	Anionic Nanoemulsion	0.1% v/v in 6% KCl	30.10	6.17	9.5
FBE-C	Anionic Nanoemulsion	0.2% v/v in 6% KCl	28.47	2.79	9.2

formed was also measured by dynamic light scattering by adding 0.1% to 0.2% of FBE in 6% KCl. Table 3 also shows that the size of emulsion was smaller than 10 nm for the prepared flow back enhancers. The size of the emulsion droplet proved the formation of the oil-in-water nanoemulsion.

Contact Angle

The wetting characteristics of flow back enhancers on a glass surface was evaluated by the contact angle method. The glass slides were flame treated before conducting the tests to remove any dust and organic materials. Table 4 lists the contact angle of the 0.2% v/v flow back additive in 6% KCl on heat cleaned glass slides and the contact angle of water on pretreated glass slides with 0.2% v/v flow back additive in 6% KCl.

Most of the contact angles were below 23.5° pointing to a water-wet surface. After the glass slides were pretreated with 0.2% v/v of flow back additive in 6% KCl and dried in an oven, the contact angle was measured with DI water. The contact angle for most of the fluids changed only a little bit, except FBE-C, which moved from 16.3° to 45°. The flow back enhancer FBE-C changed the wettability of the glass slide to a higher value.

Table 4 *The contact angle of 0.2% v/v flow back additive in 6% KCl on heat cleaned glass slides; and the contact angle of water on pretreated glass slides with 0.2% v/v flow back additive in 6% KCl.*

Flow Back Enhancer	Heat Cleaned Glass Slide	Pretreated Glass Slide
6% KCl	4.6	4.8
FBE-A	14.6	10.5
FBE-B	16.7	16.3
FBE-C	16.3	45.0

Since FBE-A and FBE-B contained a linear ethoxylated alcohol-based surfactant as demulsifiers, that kept the surface hydrophilic, which is good for oil recovery. At the same time, it lowers the surface tension and IFT that is good for flow back of fracturing fluid and oil production. Changing the contact angle to a higher value and closer to 90° is important to make the surface of the formation non-wetting, which is good for production of both oil and water, and the prevention of oil and water from blocking the formation. FBE-C with a contact angle of 45° is good for prevention of oil and water from blocking the formation.

Emulsion Breaking

One of the functions of a flow back enhancer is to prevent the formation of emulsion between the formation oil and the fracturing fluid. Without flow back enhancers, the fracturing fluid can form water-in-oil emulsion with the crude oil, which can plug the formation or reduce the production of oil. The flow back enhancers are formulated to prevent the formation of emulsions or to demulsify an emulsion that has been formed. To accomplish this task, a demulsifier such as alcohol ethoxylate, PEG-PPG-PEG and castor oil ethoxylates with HLB in the range from 10 to 16 are used in the formulations.

Emulsion break tests were conducted to test the effectiveness of the flow back enhancers at preventing an emulsion formation between the crude oil and fracturing fluid. The aqueous broken slick water fracturing fluid without any flow back enhancer was shaken with crude oil at a ratio of 1:1 to observe the formation of emulsion. This serves as the control test for the emulsion formation. The emulsion was kept at room temperature for 15 minutes to observe the separation of the aqueous and oil phase. After that, the emulsion was heated at 65.55 °C (150 °F) for 40 minutes and photographed at set intervals to observe separation. It was observed that no demulsification was achieved in 1 hour.

Similarly, the experiments were conducted with a 0.2% v/v of flow back enhancer in a broken slick water fluid formed in 6% KCl and shaken with crude oil. The emulsion formed was then left at room temperature for 15 minutes followed by heating at 65.55 °C for 40 minutes. The separation of oil and aqueous phase was observed and photographed.

Table 5 shows that when there was no flow back enhancer present, the broken fracturing fluid formed a tight emulsion with crude oil and no separation was observed at room temperature or at 65.55 °C within 1 hour. Whereas, when the developed flow back enhancers were added at a 0.2% v/v concentration, the emulsion started breaking at room temperature within 15 minutes. Heating at 65.55 °C allowed the aqueous phase and oil phase to separate into two distinct layers. In some cases, a yellow color was observed in the aqueous phase, which was due to some oil-in-water emulsion.

Depending on the crude oil and its constituents (wax, acidity, or basicity, etc.) it will be required to adjust the demulsifier present in the flow back enhancer to a lower HLB so as not to form oil-in-water emulsion. The higher temperature in some wells will also help in the breaking of emulsions at a faster rate and the oil water interface was a crisp layer, indicating a little emulsion at the interface.

Gravity Drainage Fluid Recovery Column Test

In this test, a small column was packed with SafeCarb 250 carbonate particles (250 to 300 microns), and then the column was treated with 3 PVs of fluid containing 0.2% v/v of flow back enhancer in a 2% KCl solution. After the drainage of 3 PVs of the fluid, crude oil was added on top of the column to displace the aqueous fluid containing a flow back enhancer from the pore spaces of the packed column.

A successful treatment was one that allowed quick displacement of the water phase containing the flow back

Table 5 *The emulsion break test of the emulsion formed between the broken slick water fracturing fluid prepared in 6% KCl with crude oil (ratio of 1:1) containing 0.2% v/v of flow back enhancer. The emulsified sample is kept at room temperature for 15 minutes followed by 40 minutes at 150 °F in a water bath.*

	Room Temperature			65.55 °C (150 °F)					
Time	**5**	**10**	**15**	**5**	**10**	**15**	**20**	**30**	**40 min**
Broken fracture fluid crude oil without FBE (ratio 1:1)									
Broken fracture fluid 0.2% v/v FBE-A crude oil (ratio 1:1)									
Broken fracture fluid 0.2% v/v FBE-B crude oil (ratio 1:1)									
Broken fracture fluid 0.2% v/v FBE-C crude oil (ratio 1:1)									

enhancer fluid followed by quick oil breakthrough in comparison to a control treatment of 2% KCl followed by crude oil. A greater displacement volume early in the drainage test was considered an advantage as it translates to quick recovery of load and increased hydrocarbon production.

Figure 4 shows the results from the gravity drainage column test. In this test the three developed flow back enhancers, FBE-A, FBE-B, and FBE-C, were used at a concentration of 0.2% v/v in 6% KCl. Crude oil was used as the displacement fluid. A control experiment was done with 6% KCl fluid without any flow back enhancer. As seen in Fig. 4, the control fluid gave an initial "spurt" of displaced brine and then stopped draining, resulting in a near flat response for the remaining time in comparison to the other test results.

The best performing flow back enhancer from this test was FBE-C, which had a breakthrough of crude oil after 900 seconds and an aqueous fluid displacement of 98%. The two-phase flow after oil breakthrough had an upward trending line that shows it increased the rate of brine and oil flow through the column. The FBE-B saw oil breakthrough after 945 seconds with an aqueous brine fluid displacement of 70% at the oil breakthrough point. In all these experiments, the clear winner was the anionic flow back enhancer FBE-C followed by FBE-B.

Similarly, the gravity drainage test is conducted with an 80/100 mesh sand packed column with a 0.2% v/v flow back enhancer, FBE-A, FBE-B, and FBE-C, in 6% KCl with displacement with crude oil. Figure 5 shows the results from the gravity drainage column test. A control experiment was done with 6% KCl fluid without any flow back enhancer.

The best performing flow back enhancer from this test was FBE-C, which had an early breakthrough of crude oil within 300 seconds. The two-phase flow after oil breakthrough had an upward trending line that shows it increased the rate of brine and oil flow through the column. FBE-B saw oil breakthrough after 1,100 seconds. FBE-B had approximately 80% brine drainage before the two-phase flow started. FBE-A took around 1,500 seconds for oil breakthrough with 100% brine recovery. But the oil recovery after that slowed down. In all of these experiments, the clear winner was the anionic flow back enhancer FBE-C.

Fig. 4 *The gravity drainage fluid recovery column test result with 0.2% v/v flow back enhancer in a 6% KCl followed by crude oil using a SafeCarb 250 packed column.*

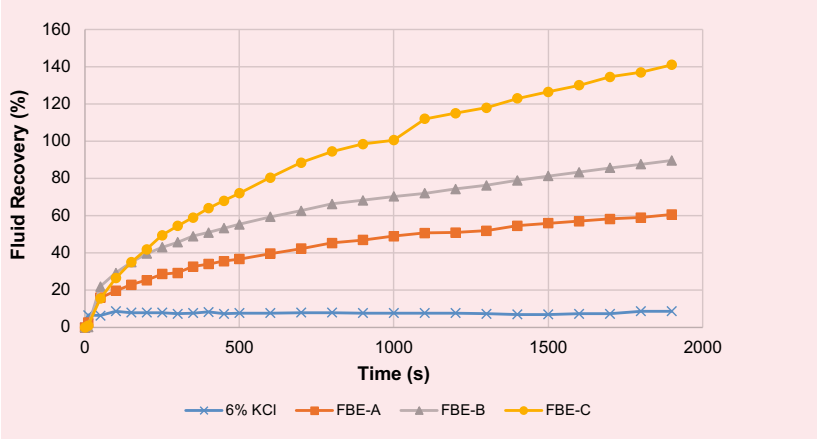

Fig. 5 *The gravity drainage fluid recovery column test results with 0.2% v/v flow back enhancer in a 6% KCl followed by crude oil using 80/100 mesh sand pack.*

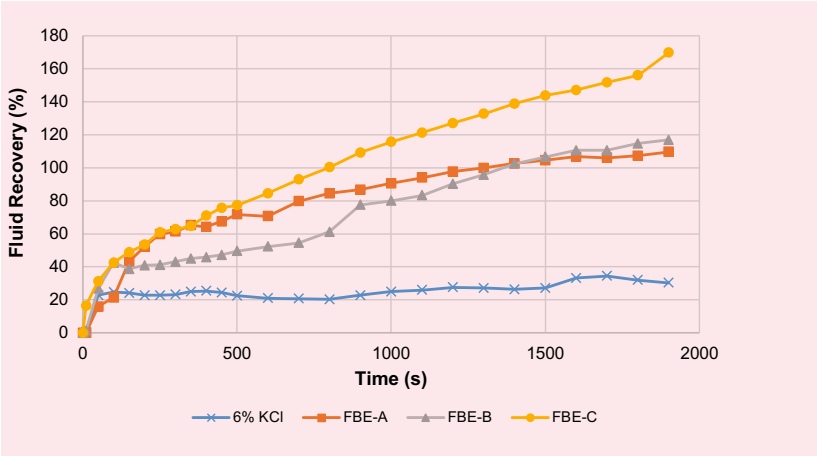

Amott Cell Imbibition Test

In the Amott cell experiment, Indiana Limestone cores were saturated with kerosene oil under vacuum. Kerosene was used as a substitute for crude oil. Based on the difficulty of procuring crude oil, the differences in crude oils from various locations, as well as how the composition of crude oil can change over time, it was concluded that it was best to use a reference fluid for the tests. Further research is planned for each target crude oil.

A test fluid of 6% KCl containing 0.2% v/v of flow back enhancer was used to run the experiment at room temperature for 24 hours while the displaced kerosene from the core was measured. Figure 6 shows that when no flow back enhancer was present in the 6% KCl fluid solution, the core released kerosene oil very slowly and only reached a recovery of 32% in 24 hours.

As seen from most of the flow back enhancer tests, the maximum amount of oil displacement occurred in the first 20 minutes of the core immersion in the flow back enhancer fluid, followed by small releases in the next 24 hours. When referring to the IFT results in Table 3, the product with the lowest IFT did not result in the best oil production. It seems it also depends on other factors such as mineralogy, wettability, and interaction with surfactants and brines. The best kerosene recovery was obtained using flow back enhancer FBE-B followed closely by FBE-C with an ultimate recovery of 56% and 55%, respectively. FBE-A provided a recovery of approximately 49%.

Similarly, Amott cell imbibition tests were done on Berea buff sandstone cores saturated with kerosene oil under vacuum. A treatment fluid of 6% KCl containing

0.2% v/v of flow back enhancer was used to run the experiment at room temperature for 24 hours and the displaced kerosene from the core was measured.

Figure 7 shows that when no flow back enhancer was present in the 6% KCl fluid solution, the released kerosene oil from the core was very slow and only reached a recovery of 32% in 24 hours. As seen from most of the flow back enhancer tests, the maximum amount of oil displacement occurred in the first 20 minutes of the core immersion in the flow back enhancer fluid followed by a small release in next 24 hours.

When referring to the IFT results in Table 3, the product with the lowest IFT did not result in the best oil production. The best kerosene recovery was obtained using flow back enhancer FBE-C, an anionic nanoemulsion and a cationic flow back enhancer FBE-B of 59% and 56%, respectively. Other flow back enhancers provided oil recovery of approximately 46% to 50%.

Core Flow Regained Permeability Test

Several core flow experiments were performed to compare the nanoemulsion flow back enhancers developed to improve relative permeability and fluid recovery in the presence of kerosene and broken fracturing fluid. Austin chalk was chosen to use for the core flow tests. The permeability for these cores was at the correct range to provide adequate differential pressure across the core while still being able to maintain a pumping rate of at least 1 mL/min.

The tighter cores of the same size require the pumping rates to be too slow. Broken fracture fluid is used for testing because the intent is to test the effect of the treatment on the core matrix. The slick water broken fracture fluid was used as the treatment stage in the core flow tests and kerosene was used for the initial and final regained permeability test using the Austin chalk cores.

Three different nanoemulsion solutions (FBE-A, FBE-B, FBE-C) were tested to compare the effectiveness of these solutions in improving oil permeabilities in carbonate cores. Initial permeability was measured by injecting kerosene at 3 mL/min through the core at temperature of 93.33 °C (200 °F) until the pressure was stabilized. The results from Table 5 showed that the initial oil permeability of the cores used in the test were between 5 md to 30 md. The core was then injected with 2 PVs of broken slick water fluid containing 0.2% v/v of flow back enhancer. The core was then maintained at room temperature overnight — for 16 hours — to mimic the time between treatment and flow back. The regained permeability was measured by injecting kerosene in the production direction at 3 mL/min until a stable reading was obtained. The regained permeability data for the Austin chalk core flow tests are given in Table 6.

The control permeability was also measured by injecting broken slick water fluid without any flow back enhancer and then measuring the regained permeability by injecting kerosene in the same way as done for the broken slick water fluid containing a flow back enhancer, Fig. 8. In the control experiment, the initial permeability of the core with kerosene was found to be 16.6 md. After the injection of 2 PVs of broken slick water fluid without the addition of a flow back enhancer, the final regain permeability with kerosene was found to be 9.4 md. In the control experiment, a regained permeability of 56.6% was obtained.

Fig. 6 *Kerosene displacement over 24 hours using 0.2% v/v flow back enhancer in a 6% KCl solution from kerosene saturated Indiana limestone.*

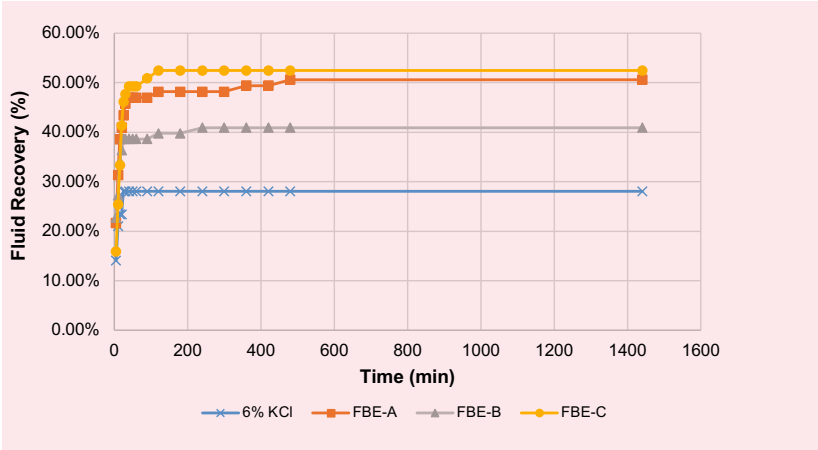

Fig. 7 *Kerosene desorption over 24 hours using 0.2% v/v flow back enhancer in a 6% KCl solution from kerosene saturated Berea sandstone.*

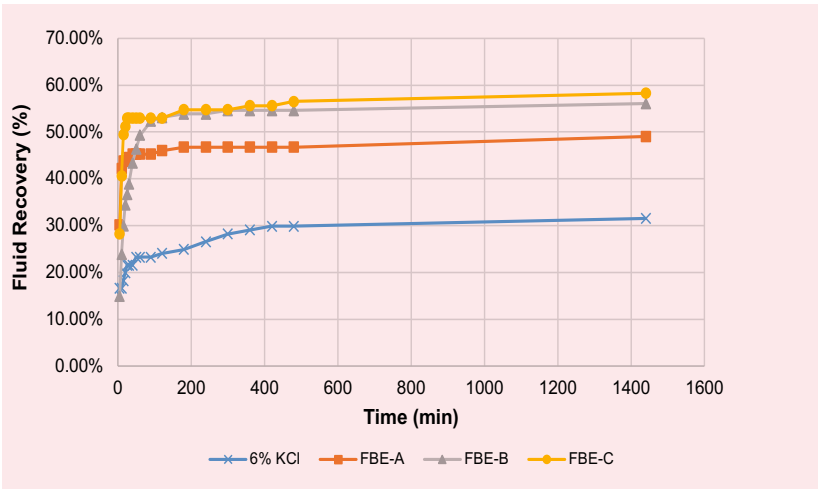

Table 6 also shows that the regained permeability of the control sample was 56.6% whereas the broken slick water fracturing fluid containing FBE-A, FBE-B, and FBE-C is 70%, 75%, and 64%, respectively. From these tests it can be clearly seen that all the treatments with flow back enhancer fared better than the control sample. Also, the FBE-B at 75% regained is the best flow back enhancer in terms of regain permeability.

In the column testing, FBE-C fared better than FBE-B, but in Amott cell and core flow testing of FBE-B fared better than FBE-C. Consequently, the results from the Amott cell and core flow test can be within experimental errors. It is fair to say that FBE-B and FBE-C both

Table 6 *The Austin chalk core flow results using a 0.2% v/v flow back enhancer in a broken slick water fluid at 93.33 °C (200 °F).*

Test	Flow Back Enhancer in Broken Slick Water Fluid (2 gpt)	Initial Permeability (md)	Regained Permeability (md)	Regained Permeability (%)
1	Control (no flow back)	16.6	9.4	56.6
2	FBE-A	19.6	13.7	69.9
3	FBE-B	9.2	6.9	75.0
4	FBE-C	24.7	15.9	64.3

Fig. 8 *The control regained permeability test using broken slick water fluid without a flow back enhancer.*

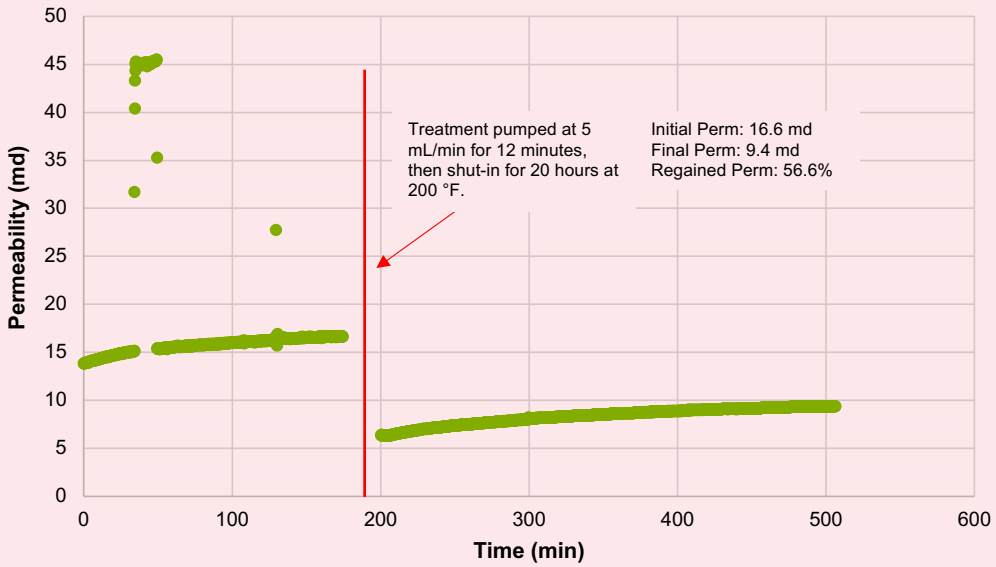

Fig. 9 *The regained permeability test using broken slick water fluid containing 0.2% v/v of FBE-A.*

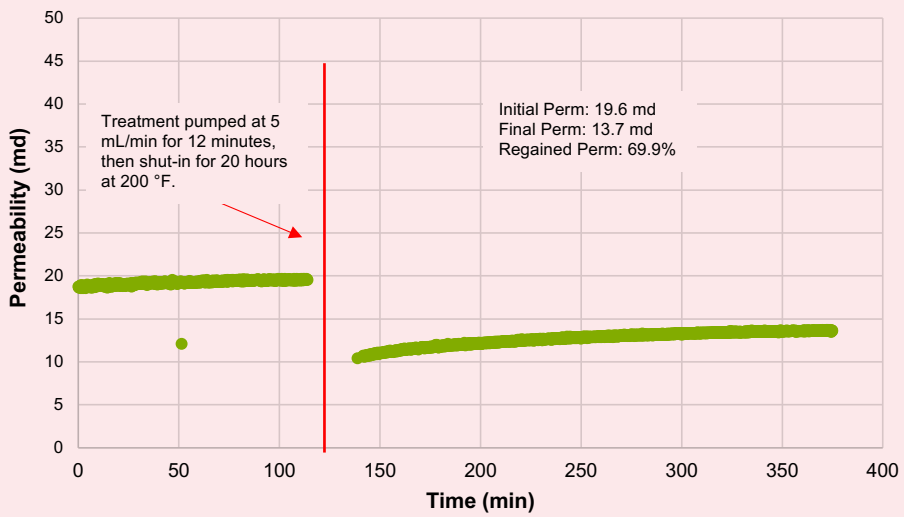

Fig. 10 *Regained permeability test using broken slick water fluid containing 0.2% v/v FBE-B.*

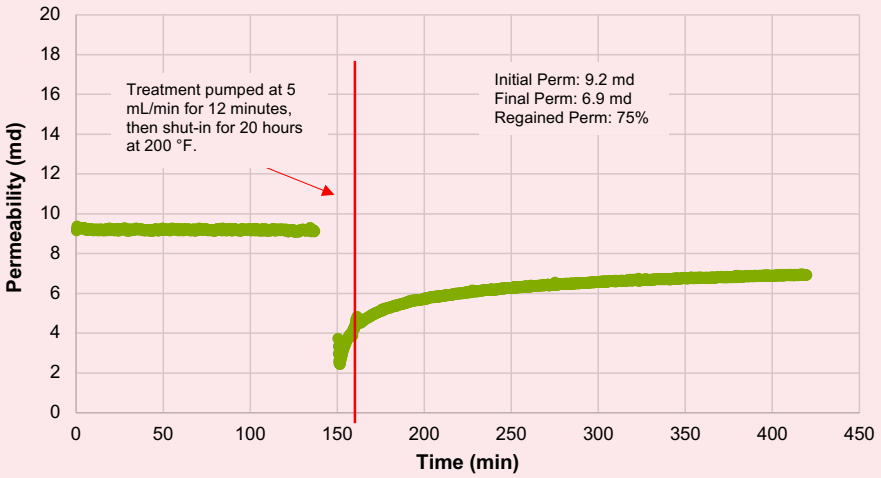

Fig. 11 *Regained permeability test using broken slick water fluid containing 0.2% v/v FBE-C.*

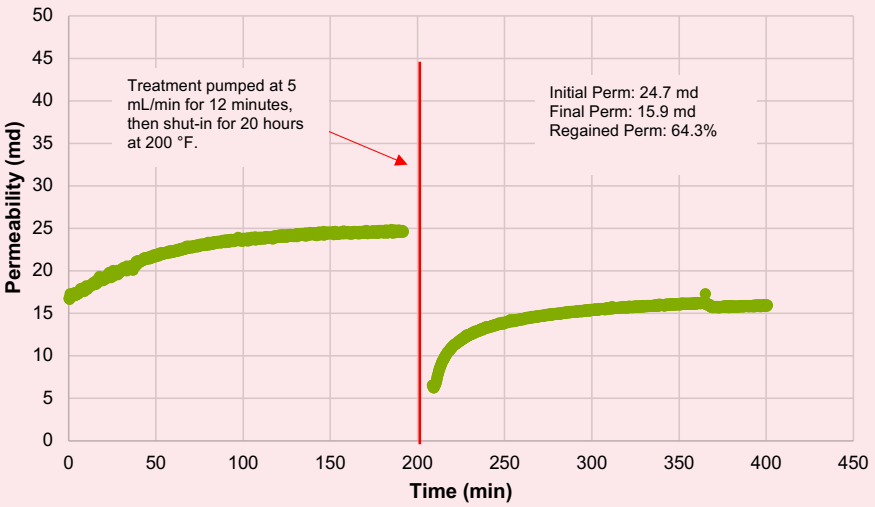

fared well with the carbonate formation containing oil. The graphs of the core flow tests for all of the flow back enhancers is presented in Figs. 8 to 11.

Similarly, core flow studies were done using Berea sandstone using a 0.2% v/v flow back enhancer in 6% KCl with FBE-A, FBE-B, and FBE-C. The slick water broken fracture fluid was used in the core flow tests and kerosene was used for the initial and final regained permeability test using Berea sandstone. The results from Table 7 showed that the initial oil permeability of cores used in the test were between 5 md to 15 md. The core was then injected with 2 PVs of broken slick water fluid containing 0.2% v/v of flow back enhancer.

In the control experiment, the initial permeability of the core with kerosene was found to be 11 md. After the injection of 2 PVs of broken slick water fluid without the addition of a flow back enhancer, the core was allowed to sit at room temperature overnight for 16 hours. Afterwards, the final regain permeability with kerosene was found to be 4.54 md. In the control experiment, a regained permeability of 41% was obtained. Table 7 also shows that the regained permeability by using a flow back enhancer is greater than when the broken fluid is used without any flow back enhancer in the Berea sandstone core flow tests.

On the basis of the presented results, a lower surface tension, IFT, and formation contact angle does not translate into better fluid recovery and production. There is still a need for the better understanding of formation minerology, crude oil properties, and their interactions

Table 7 *The Berea sandstone core flow test results using a 0.2% v/v flow back enhancer in a broken slick water fluid at 93.33 °C (200 °F).*

Test	Flow Back Enhancer in Broken Slick Water Fluid (2 gpt)	Initial Permeability (md)	Regained Permeability (md)	Regained Permeability (%)
1	Control (no flow back)	11.0	4.5	41
2	FBE-A	8.9	6.5	73
3	FBE-B	14.5	9.1	62
4	FBE-C	10.8	8.2	75

with the different surfactants for optimum fluid recovery and hydrocarbon production.

Conclusions

Three nanoemulsion-based flow back enhancers (FBE-A, FBE-B and FBE-C) were formulated and tested by measuring their characteristics (surface tension, IFT, contact angle, and emulsion droplet size) and performance (gravity drainage column flow test, emulsion test, Amott imbibition test, and core flow permeability test).

All flow back enhancers gave very low surface tension and IFT required for lowering the capillary pressure.

The flow back enhancers' emulsions have a size smaller than 9.2 nm, which is able to penetrate smaller pore spaces in tight formations.

All of the three flow back enhancers prevented the formation of emulsion with crude oil.

From all the performance results it can be concluded that FBE-C is superior in the column flow test, the FBE-B is superior in core flow tests, and the Amott cell tests both have similar results within an experimental error rate.

It can be concluded that FBE-C provided superior performance in the oil-bearing carbonate and sandstone formations followed closely by FBE-B.

Nanoemulsions have a great potential for enhancing fracturing fluid and oil recovery in oil-bearing carbonate reservoirs.

References

1. Cawiezel, K.E., Singh, A.K., Carman, P.S. and Cutler, J.L.: "The Selection and Optimization of a Surfactant Package to Maximize Cleanup of High-Density Fracturing Fluid," SPE paper 136812, presented at the SPE Deepwater Drilling and Completions Conference, Galveston, Texas, October 5-6, 2010.

2. Kaufman, P.B., Penny, G.S. and Paktinat, J.: "Critical Evaluations of Additives Used in Shale Slick Water Fracs," SPE paper 119900, presented at the SPE Shale Gas Production Conference, Fort Worth, Texas, November 16-18, 2008.

3. Longeron, D.G., Alfenore, J. and Poux-Guillaume, G.: "Drilling Fluids Filtration and Permeability Impairment: Performance Evaluation of Various Mud Formulations," SPE paper 48988, presented at the SPE Annual Technical Conference and Exhibition, New Orleans, Louisiana, September 27-30, 1998.

4. Cuiec, L.: "Effect of Drilling Fluids on Rock Surface Properties," *SPE Formation Evaluation*, Vol. 4, Issue 1, March 1989, pp. 38-44.

5. Penny, G.S., Pursley, J.T. and Holcomb, D.: "The Application of Microemulsion Additives in Drilling and Stimulation Results in Enhanced Gas Production," SPE paper 94274, presented at the SPE Production Operations Symposium, Oklahoma City, Oklahoma, April 16-19, 2005.

6. Audibert-Hayef, A. and Dalmazzone, C.: "Surfactant System for Water-Based Well Fluids," *Colloidal and Surfaces A: Physicochemical and Engineering Aspects*, Vol. 288, Issues 1-3, October 2006, pp. 113-120.

7. Galindo, T. and Rimassa, S.: "Evaluation of Environmentally Acceptable Surfactants for Application as Flowback Aids," SPE paper 164122, presented at the SPE International Symposium on Oil Field Chemistry, The Woodlands, Texas, April 8-10, 2013.

8. Zhang, H., Marinescu, P. and Foxenberg, W.: "Unique Flow Back Chemistry for Enhancing Productivity of Low Permeability Reservoir," SPE paper 155505, presented at the IADC/SPE Asia Pacific Drilling Technology Conference and Exhibition, Tianjin, China, July 9-11, 2012.

9. Al-Anazi, M.S., Al-Khaldi, M.H., Fuseni, A. and Al-Marshad, K.M.: "Use of Nanoemulsion Surfactants during Hydraulic Fracturing Treatments," SPE paper 171911, presented at the Abu Dhabi International Petroleum Exhibition and Conference, Abu Dhabi, UAE, November 10-13, 2014.

10. Mahmoudkhani, A., O'Neil, B., Wylde, J.J., Kakadjian, S., et al.: "Microemulsion as Flowback Aids for Enhanced Oil and Gas Recovery after Fracturing, Myth or Reality: A Turnkey Study to Determine the Features and Benefits," SPE paper 173729, presented at the SPE International Symposium on Oil Field Chemistry, The Woodlands, Texas, April 13-15, 2015.

11. Kim, J., Zhang, H., Sun, H., Li, B., et al.: "Choosing Surfactants for the Eagle Ford Shale Formation: Guidelines for Maximizing Flowback and Initial Oil Recovery," SPE paper 180227, presented at the SPE Low Perm Symposium, Denver, Colorado, May 5-6, 2016.

12. Yue, Z., Peng, Y., He, K. and Xu, L.: "Multifunctional Fracturing Additives as Flowback Aids," SPE paper 181383, presented at the SPE Annual Technical Conference and Exhibition, Dubai, UAE, September 26-28, 2016.

13. Himes, R., Lansford, M.L. and Snider, J.: "Improved Method to Evaluate Flowback Additives for Frac Fluids Used in Unconventional Reservoirs," SPE paper 187200, presented at the SPE Annual Technical Conference and Exhibition, San Antonio, Texas, October 9-11, 2017.

14. Nelson, C.W., Hilliard, C., Kalantar, T.H., Li, Y., et al.: "A Novel High throughput Screening Approach for Flowback Aid Optimization," SPE paper 189552, presented at the SPE International Conference and Exhibition on Formation Damage Control, Lafayette, Louisiana, February 7-9, 2018.

About the Authors

Dr. Rajesh K. Saini

Ph.D. in Organic Chemistry, Kurukshetra University

Dr. Rajesh K. Saini is a Research Science Specialist working with the Production Technology Team at the Aramco Research Center-Houston. He has more than 24 years of experience in the oil and gas industry, and chemical research. Rajesh is a subject matter expert in oil field stimulation, production and operations technology. He specializes in product development, scaling up, intellectual property, sales and commercialization of new products/processes for hydraulic fracturing, sand control, acidizing, production technology, oil field chemicals, and water conformance.

Prior to joining Aramco in 2017, Rajesh played critical roles at Halliburton, Weatherford, and Lubrizol in the capacity from Research Scientist to R&D Manager.

He has served as a technical reviewer for major journals, including the *Journal of American Chemical Society*, and the *Journal of Organic Chemistry and Organic Letters*. Rajesh is a Technical Editor for the Society of Petroleum Engineers (SPE) *Production and Operations Journal*. He is serving on the SPE Annual Technical Conference and Exhibition (ATCE) well stimulation committee. Rajesh holds 60 U.S. patents, 23 U.S. patent applications, and has published one book chapter and 54 peer-reviewed journal articles.

He served as the Distinguish Lecture's Program Chair and Director of the SPE-Southwest Oklahoma Section during 2009-2012. Rajesh received the Maximizing Value-Added Performance (MVP) award at Halliburton for developing environmental fracturing fluid (CleanStim®) and breaker for AquaLinear® fluid. In 2018, he was also awarded the SPE Gulf Coast Regional award for Production and Operations.

Rajesh received his MBA from Oklahoma State University, Stillwater, OK, and his Ph.D. degree in Organic Chemistry from Kurukshetra University, Haryana, India. He was a postdoctoral fellow at Rice University working with Prof. W.E. Billups and Richard E. Smalley (Nobel Laureate in Chemistry).

Brady Crane

B.S. in Chemistry, University of Science and Arts of Oklahoma

Brady Crane is a Laboratory Technician Specialist with the Production Technology Team at the Aramco Research Center-Houston. He has more than 12 years of experience in the oil and gas industry. Brady's specialties include equipment and experiment design, core flow testing, acidizing, and fracturing fluids.

Prior to joining the Production Technology Team in 2018, he spent 10 years working for service companies Halliburton and Frac Tech.

Brady has been an active member of the Society of Petroleum Engineers (SPE) for over 10 years, presenting at multiple international conferences.

He received his B.S. degree in Chemistry from the University of Science and Arts of Oklahoma, Chickasha, OK, and an MBA from Sam Houston State University, Huntsville, TX.

Nicole R. Shimek

B.S. in Biomedical Science, Texas A&M University

Nicole R. Shimek is a Lab Technician Specialist with the Production Technology Team at the Aramco Research Center-Houston. She has almost 10 years of experience in the oil and gas industry, and chemical research. Nicole specializes in product development and testing for fracturing, acidizing, production technology, and oil field chemicals.

Prior to joining the Production Technology Team in 2019, she played critical roles at Weatherford and Lubrizol in the capacity of a Technical Lab Specialist.

Nicole's key expertise has been in acid corrosion, acid emulsions, acid gelling agents, anti-sludge agents, iron control additives, and non-emulsifiers. She currently holds two patents in her expertise for continuous mixed emulsified acids and acid corrosion inhibitors.

Nicole is a member of the Society of Petroleum Engineering (SPE) and the National Association of Corrosion Engineers (NACE).

She received her B.S. degree in Biomedical Science from Texas A&M University, Corpus Christi, TX.

Dr. Weiran Wang

Ph.D. in Inorganic Chemistry, University of Texas at Austin

Dr. Weiran Wang is a Scientific Developer in the Emerald Cloud Lab. He working on the development the code interface in transferring traditional life science research tools into online services for researchers to conduct their experiments remotely. Before joining the Emerald Cloud Lab, Weiran worked as a Teaching Specialist at the University of Texas at Austin.

In the summer of 2019, he worked as a graduate intern with the Production Technology Team at the Aramco Research Center-Houston. Weiran contributed to the project related to the emulsion-based flow back aids under the mentorship of Dr. Rajesh Saini.

He is the coauthor of five articles published in peer-reviewed journal.

Weiran was awarded a professional development award for presenting his research at the 2019 American Chemical Society national meeting in San Diego, CA. He was also awarded the College of Natural Sciences Dean's Excellence Fellowship at the University of Texas at Austin.

Weiran received his Ph.D. degree in Inorganic Chemistry from the University of Texas, Austin, TX. He studied the thiophene-based functional materials under the mentorship of Dr. Richard A. Jones.

Brent Cooper

B.S. in Biology, Texas A&M University

Brent Cooper is a Lab Technician Specialist with the Production Technology Team at the Aramco Research Center-Houston. Since joining the company in 2014, his work has supported several key projects within the Production Technology Team. Brent was recognized as the recipient of the Best Team Player award in the fall of 2014.

His specialties cover a broad spectrum of both traditional analytical laboratory equipment and devices that are specifically geared toward oil and gas research.

Since joining the Center, Brent has commissioned new instruments and developed an analytical methodology for many devices throughout the Center that provides accurate data to scientists and engineers.

He received his B.S. degree in Biology from Texas A&M University, College Station, TX.

Population Balance Mechanistic Simulation of CO_2 Foam Flooding

Dr. Muhammad M. Almajid, Dr. Zuhair A. Al-Yousef, and Othman S. Swaie

Abstract /

Mechanistic modeling of the non-Newtonian carbon dioxide (CO_2) foam flow in porous media is a challenging task that is computationally expensive due to abrupt gas mobility changes. The objective of this article is to present a local equilibrium CO_2 foam mechanistic model, which could alleviate some of the computational cost, and its implementation in the MATLAB reservoir simulation tool (MRST). Interweaving the local equilibrium foam model into MRST enables users' quick prototyping and testing of new ideas and/or mechanistic expressions.

We use MRST, the open source tool available from SINTEF, to implement our local equilibrium foam model. The model utilizes the MRST automatic differentiation capability to compute the fluxes as well as the saturations of the aqueous and gaseous phases at each Newton iteration. These computed variables and fluxes are then fed into the local equilibrium foam model that estimates the bubble density — number of bubbles per unit volume of gas — in each grid block. Finally, the estimated bubble density at each grid block is used to readjust the gaseous phase mobility until convergence is achieved.

Unlike the full-physics model, the local equilibrium foam model does not add a population balance equation for the flowing bubbles. The developed local equilibrium foam model, therefore, does not add much computational cost to solving a black oil system of equations as it uses the information from each Newton iteration to adjust the gas mobility. Our model is able to match experimental transient foam flooding results from the literature. The chosen flowing foam fraction (*Xf*) formula dictates to a large extent the behavior of the solution. An appropriate formula for *Xf* needs to be chosen, such that our simulations are more predictive.

The work described in this article could help in prototyping various ideas about the generation and coalescence of bubbles, as well as any other correlations used in any population balance model. The chosen model can then be used to predict foam flow and estimate the economic value of any foam pilot project.

Introduction

The mobility ratio between the displacing and displaced fluids plays a major role in determining the sweep behavior during any reservoir flood[1]. When you have a more viscous fluid displacing a less viscous one, you will have a piston-like displacement. Reverse the fluids and you will end up with displacing a small amount of the resident fluids. During gas injection in porous media, we tend to have a less viscous fluid displacing a more viscous one[2]. Therefore, the displacement ends up being nonuniform and lots of fingering ensues.

Foaming the injected gas is an effective method in controlling its mobility[3, 4]. Foam is defined as a dispersion of gas in a liquid in which the liquid is typically surfactant-laden water. The aqueous phase of the foam is continuous in porous media as it coats the rock grains, as well as separates the discontinuous gaseous phase[4, 5]. The gas bubbles are separated by thin liquid films that are called lamellae. Because the gas phase is discontinuous, it is apparent that the viscosity increases since you have to overcome the resistance of the lamellae before foam moves[6]. Additionally, some of the gas will be trapped, which will affect its relative permeability[5, 7].

These two factors combine to lower the gas mobility to more favorable values. Foam has been implemented in the field for many purposes, such as mobility control during enhanced oil recovery (EOR) projects, remediation jobs, acid/stimulation (diversion) jobs, and hydraulic fracturing. Due to its popularity and applicability for many field operations, it is important to be able to predict the foam's behavior in porous media accurately.

The essence of any foam simulator is that it adjusts the gas mobility somehow to represent the foamed gas mobility. This is typically done by computing or estimating the bubble density — number of bubbles per unit volume of gas — that is also known as foam texture. Ma et al. (2015)[8] provides a comprehensive review of simulation techniques and their characteristics. They categorize foam simulation techniques into three categories: (1) Population balance models, (2) local equilibrium models, and (3) other approaches that include percolation theory models/network models[8].

Some of these techniques are applicable to some scales, but not others. For instance, the percolation theory was used to simulate foam flow in pore networks[9, 10], which is a much smaller scale than where population balance models where used, e.g., in corefloods/field scale[11, 12]. Furthermore, Ma et al. (2015)[8] subcategorize population balance models into three versions: (1) dynamic texture version, (2) local equilibrium version, and (3) implicit texture version.

Commercial simulators such as Eclipse or CMG uses the implicit texture version where correlations are used to code in some physical behavior that has been observed into factors. These factors are then combined to derive a foam reduction factor, which is multiplied by the gas mobility to adjust it to the foam mobility. The problem with such models is that the parameters are usually hard to interpret and are not necessarily physical. The other two categories are more mechanistic and their parameters usually have direct relationships with experimental observations.

A mechanistic model is one that takes observed experimental mechanisms into account. It is the natural way of predicting any physical behavior. It provides a framework for numerical experimentation that allows sensitivity studies to be performed. It can, therefore, direct researchers into which parameters are more important to focus on or study in detail. Additionally, it is relatively easier to unravel the dependencies of its different parameters compared to other types of foam models. Therefore, we can study in detail what one parameter alters if it is changed and how the displacement behavior responds to changes in various parameters.

This article details a local equilibrium mechanistic foam model to simulate foam flow in porous media. We show an application to carbon dioxide (CO_2) foam, but predicting nitrogen (N_2) foam can be achieved using the same developed model. The local equilibrium model is based on physical, observed mechanisms, and therefore, is built ground up from pore level phenomena. We use the open-source MATLAB reservoir simulation toolbox (MRST) from SINTEF because it allows flexibility for implementation and it offers automatic differentiation capability. The implemented foam model in MRST provides a platform for quick prototyping of new formulas or new physics.

This article proceeds by reviewing the theory that is used to rationalize the model used. In the theory section, we justify the use of the local equilibrium model. Then, we present the results we obtained and compare them with experimental data from the literature. We follow that with a conclusion that includes potential extensions and remaining open questions.

Theory

Bubbles are separated by thin liquid films that are called lamellae. Each lamella provides a resistance to flow[6, 13]. Many studies confirm the dependence of foam flow on bubble density[9, 11]. For instance, the pore network analysis of Almajid and Kovscek (2020)[9] confirms that foam flow differs as the snap-off probability (f_{so}) increases. As the f_{so} increases, the number of lamellae in the porous medium becomes larger, therefore the bubble density increases, too. Their study, as well as many others, suggest that to model foam flow accurately, the bubble density needs to be considered.

Population balance models track the changes in bubble density, n_f, dynamically by adding a conservation equation for the bubble density. The assumption is that the flowing bubbles flow only with the gaseous phase. The conservation equation for them is written as:

$$\frac{\partial}{\partial t}\left[\phi\left(S_{gf}n_f + S_{gt}n_t\right)\right] + \nabla\cdot\left(u_f n_f\right) = \phi S_g\left(k_1|v_w||v_f|^{\frac{1}{3}} - k_{-1}|v_f|n_f\right) + Q_b \quad (1)$$

where S_{gf} is the flowing gas saturation, S_{gt} is the trapped gas saturation, n_f the flowing bubble density, n_t the trapped bubble density, u_f is the Darcy velocity of the gas with the modified mobility due to the presence of foam, ϕ the porosity, k_1 the generation constant, k_{-1} the coalescence constant, v_w the interstitial water velocity, v_f the interstitial gas velocity, and Q_b the source/since term of any preexisting bubbles.

Notice that we have used the rate of generation definition[11]. The rate of generation is linearly proportional to the liquid phase velocity and has a power-law relationship with respect to the gaseous phase. The generation rate constant we use is the one proposed[11] that is applicable to both the high and low quality regimes:

$$k_1 = k_1^0\left[1 - \left(\frac{n_f}{n_f^*}\right)^{\omega}\right] \quad (2)$$

where k_1^0 is a constant of proportionality, n_f^* is an upper limit of the bubble density that is related to pore size, and ω is a constant that determines the shape of the inverse proportionality of foam generation sites.

The rate of coalescence in Eqn. 1 is proportional to the flux of the bubbles into termination sites in the porous media. Termination sites are those that have characteristics that would destroy the lamellae. k_{-1} is the coalescence constant that depends on the porous medium capillary pressure, the limiting capillary pressure of the surfactant, and the concentration of the surfactant used. The foam coalescence constant is written as:

$$k_{-1} = k_{-1}^0\left[\frac{P_c(S_w)}{P_c^*(C_s) - P_c(S_w)}\right]^2 \quad (3)$$

where $P_c(S_w)$ is the capillary pressure of the porous medium, which is a function of the water saturation. $P_c^*(C_s)$ is the limiting capillary pressure of the surfactant, which is a function of the surfactant concentration[14]. k_{-1}^0 is a constant of proportionality.

The coalescence of foam lamellae in the porous medium occurs due to the fast influx of the bubbles that causes stretching/expanding and eventual rupture[15, 16]. In addition, coalescence of lamellae could be due to the low wetting liquid content[17] or the low surfactant concentration used[18]. If the wetting content is low, the capillary pressure of the system is large. This would increase the rate of coalescence, Eqn. 3. Similarly, if the limiting capillary pressure is small, due to the properties or concentration of the surfactant used, then k_{-1} increases, too.

Upon the appearance of lamellae in the system, the multiphase parameters change. Specifically, the viscosity of the gas appears to be greater than expected and the relative permeability of the gas seems to be smaller than usual. To capture the effect of the increased bubble density on the apparent viscosity of the gas, we use the expression that was originally proposed by Hirasaki and Lawson (1985)[6]:

$$\mu_f = \mu_g + \frac{\alpha n_f}{|v_f|^{\frac{1}{3}}} \quad 4$$

where α is a constant of proportionality that depends on surfactant formulation and permeability, and μ_f is the apparent gas viscosity in the presence of foam. Note that the apparent viscosity increases as the bubble density increases, but is generally shear thinning at constant bubble density.

Because foam blocks a large portion of the cross-sectional area available for gas flow[5, 7], we adopt a modified stone-type relative permeability correlation similar to that of Kovscek et al. (1995)[19]. We further assume that the rock is water-wet or its wettability will be modified due to the presence of surfactants. In foam, the aqueous phase is continuous, therefore, the relative permeability to water is unchanged and can be described as:

$$k_{rw} = k^0_{rw} S_{wd} \quad 5$$

where k^0_{rw} is the endpoint water relative permeability and S_{wd} is the reduced water saturation that is defined as: $S_{wd} = (S_w - S_{wc})/1 - S_{wc})$, where S_w is the water saturation and S_{wc} is the connate water saturation. On the other hand, the gaseous phase is discontinuous, and therefore, its relative permeability is modified due to the presence of stable foam. We write the gas relative permeability when foam is present as:

$$k_{rg} = k^0_{rg} S_{gd} = k^0_{rg} X_f (1 - S_{wd}) \quad 6$$

where k^0_{rg} is the endpoint gas relative permeability and X_f is the flowing fraction of foam.

There have been several numerical studies that investigated the dependence of X_f on multiphase parameters and rock properties[9, 20]. Most agree that the X_f should be a function of the pressure gradient, the flowing bubble density, and the permeability. Tang and Kovscek (2006)[7] measured X_f experimentally and analyzed its dependence on the system parameters. They conclude that the X_f increases with the increasing pressure gradient and decreases with the increasing bubble density and/or permeability. They provide the following correlation:

$$X_f = \Psi \left[\frac{|\nabla p|}{n_f k^{1/2}} \right]^{0.4} \quad 7$$

where Ψ is a constant of proportionality and the "0.4" is a percolation exponent that is applicable for 3D lattices. By combining Darcy's law and the expression of the modified gas viscosity in the presence of foam, Luo et al. (2019)[21] deduced that the X_f is a function of the total velocity of the aqueous and the gaseous phases:

$$X_f = (1 - X_t^{max}) u_t^{4/27} \quad 8$$

where we introduced the maximum X_f to the original equation proposed. Equation 8 is consistent with other correlations and measurements of X_f that showed that it depends on the gas frontal rate[22, 23]. We use Eqn. 8 in our estimation to see how much X_f is in our simulations.

Local Equilibrium Model

Several studies have examined the steady-state behavior of foam flow[3, 24]. In these studies, the estimated steady-state bubble density is obtained by equating the rate of generation and the rate of coalescence. For transient foam flow, Chen et al. (2010)[11] proposed a local equilibrium model to model the flow instead of using the full population balance model. The motivation that supports using a local equilibrium model over a full population balance model lies in its superior computational efficiency. This might prove to be very important for large-scale computations such as those needed in field pilots/developments. Chen (2009)[25] reports a speed up factor of more than two by the local equilibrium model compared to the full physics model.

The local equilibrium model can be obtained by non-dimensionlizing Eqn. 1:

$$\frac{\partial}{\partial \tilde{t}} \left[\phi \left(S_{gf} \tilde{n}_f + S_{gt} \tilde{n}_t \right) \right] + \frac{\partial}{\partial \tilde{x}} \left(\tilde{u}_f \tilde{n}_f \right) =$$

$$\phi S_g Da_{-1} \left(\frac{Da_1}{Da_{-1}} |\tilde{v}_w| |\tilde{v}_f|^{\frac{1}{3}} - |\tilde{v}_f| \tilde{n}_f \right) \quad 9$$

where $\tilde{}$ represents the normalized variables by the appropriate characteristic dimensional variable, i.e., n_c, U_c, L, and t_c. The dimensionless numbers, D_{al} and $D_{a\text{-}l}$, are Damkohler numbers that are defined as the ratio between the time-scale of fluid motion to the time-scale of the generation/coalescence. They are written as:

$$Da_1 = \frac{t_c}{t_{1,c}} = \frac{L U_c^{\frac{1}{3}} k_1}{n_c}, \quad 10$$

and

$$Da_{-1} = \frac{t_c}{t_{-1,c}} = L k_1 . \quad 11$$

Equations 10 and 11 teaches us that when the Damkohler numbers are large, foam generation/coalescence is rapid in comparison with transport processes. Using the parameters of generation and coalescence constants and characteristic length, velocity, and bubble density of 1 m, 1.1×10^{-5} m/s, and 1×10^{11} m^{-3} gives $D_{al} = 19$, and $D_{a\text{-}l} = 17$. Because these Damkohler numbers are greater than unity, it is justifiable to use the local equilibrium model to solve the system of equations developed. Even when using the core's length (0.17 m), we obtain $D_{al} = 3$ and $D_{a\text{-}l} = 2.89$.

Consequently, we equate the rate of generation and the rate of coalescence, which gives us an algebraic equation describing the bubble density[11]:

$$n_f^{\omega} + \frac{n_f^* k_{-1} |v_f|^{\frac{2}{3}}}{k_1^0 |v_w|} n_f - n_f^{*\omega} = 0 . \quad 12$$

If we set ω to 3, then we have a cubic equation that could be solved for n_f at the given multiphase conditions. In our simulator, Eqn. 12 is only solved when there is

water and gas flowing. Additionally, because we simulate a surfactant presaturated core, we do not need to worry about the surfactant concentration. Otherwise, this should be checked before the algebraic equation is solved for n_f.

In terms of numerically implementing the local equilibrium model, Fig. 1 shows the flow chart of the process. The mobility of the gas is the only phase that is affected out of the two phases in the system. Additionally, our porous medium is presaturated with surfactant, so we do not have to check for a critical surfactant saturation that otherwise will have to be checked before estimating the bubble density in the model.

Specifically, the local equilibrium model we implement computes n_f algebraically, then modifies the gas relative permeability and viscosity. The linearized system is then solved again and checked for convergence. In the case it has not converged, the updated primary variables are used again to compute the phase of the fluxes, and the whole process is repeated until convergence is achieved.

Results

To test our local equilibrium model, we use the experimental data of Farajzadeh et al. (2009)[26], who conducted flow experiments to compare the behavior of N_2 vs. CO_2 foams in porous media at high and low pressures and high and low temperatures. In our comparison, we chose the high-pressure CO_2 foam run that they performed. Their experimental pressure was set up to be 90 bars, while the temperature was controlled to be 50 °C. At these conditions, the CO_2 is in supercritical condition or very close to that condition. Table 1 lists the rock properties and the experimental conditions.

The experimental pressure drop history is shown in Fig. 2a. The pressure drop increases as the foam is generated in the core until it reaches a maximum value at the gas breakthrough. After gas breakthrough, the pressure drop declines as the foam bubbles coalesce and less resistance to flow is sensed by the fluids. Due to the choice of surfactants that Farajzadeh et al. (2009)[26] used, the eventual pressure drop in their experiments was interestingly very similar to that of CO_2 gas.

That means that all the foam had broken down and that no resistance to flow is available after the experiment had been conducted. Table 2 lists the multiphase and foam parameters used in the local equilibrium model. We had difficulties matching this transient behavior due to the fact that the pressure drops were already too small to capture. The overall pressure drop history of the local equilibrium model mimics that of the experimental observations. The solid line in Fig. 2a represents the model output. Generally, it seems that the model is capturing the pressure drop history pretty well except for very early stages and after all the foam had broken down in the core.

As for the liquid saturation profiles that are shown in Fig. 2b, the experimental observation shows that the foam is moving in a piston-like displacement. There are some capillary end effects that can be observed in the data, especially at the outlet of the core. The model predictions of the saturation profiles also propagates in a piston-like fashion similar to the experimental observations. The other thing we notice is that the liquid saturation is decreasing spatially and temporally as if there is an expansion wave. We believe that the model outputs such behavior because of the weak foam formed

Fig. 1 *A flow chart for one time step of the full nonlinear problem.*

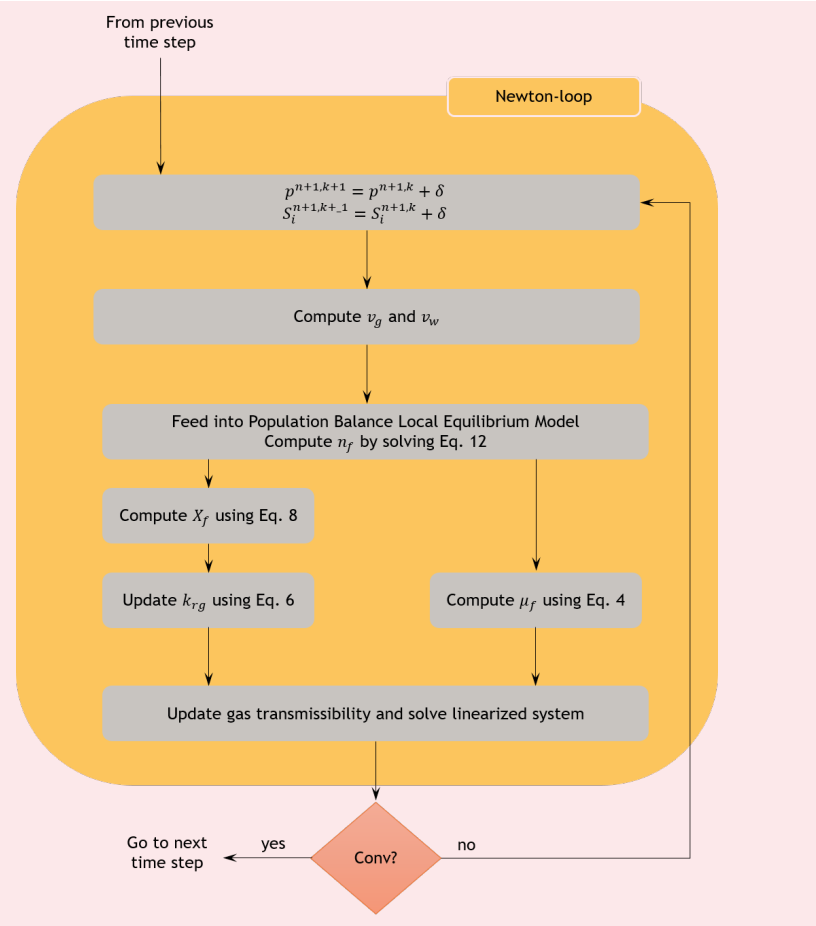

Table 1 *The rock properties and experimental conditions.*

Permeability (md)	1,100 ± 100
Porosity (%)	22 ± 0.2
Diameter (mm)	40 ± 1
Length (mm)	170 ± 2
Pore Volume (ml)	42.5 ± 0.5
Main Composition	Quartz
Back Pressure (bar)	90
Temperature (°C)	50
Flow Rate (ml/min)	1.0

Fig. 2 *The comparison between simulation and experimental results: (a) Pressure drop vs. pore volume injected, (b) water saturation profiles, and (c) computed flowing bubble density profiles. Simulation results are represented by the solid lines while experimental results with dashed lines. Experiments are taken from Farajzadeh et al. (2009)[26].*

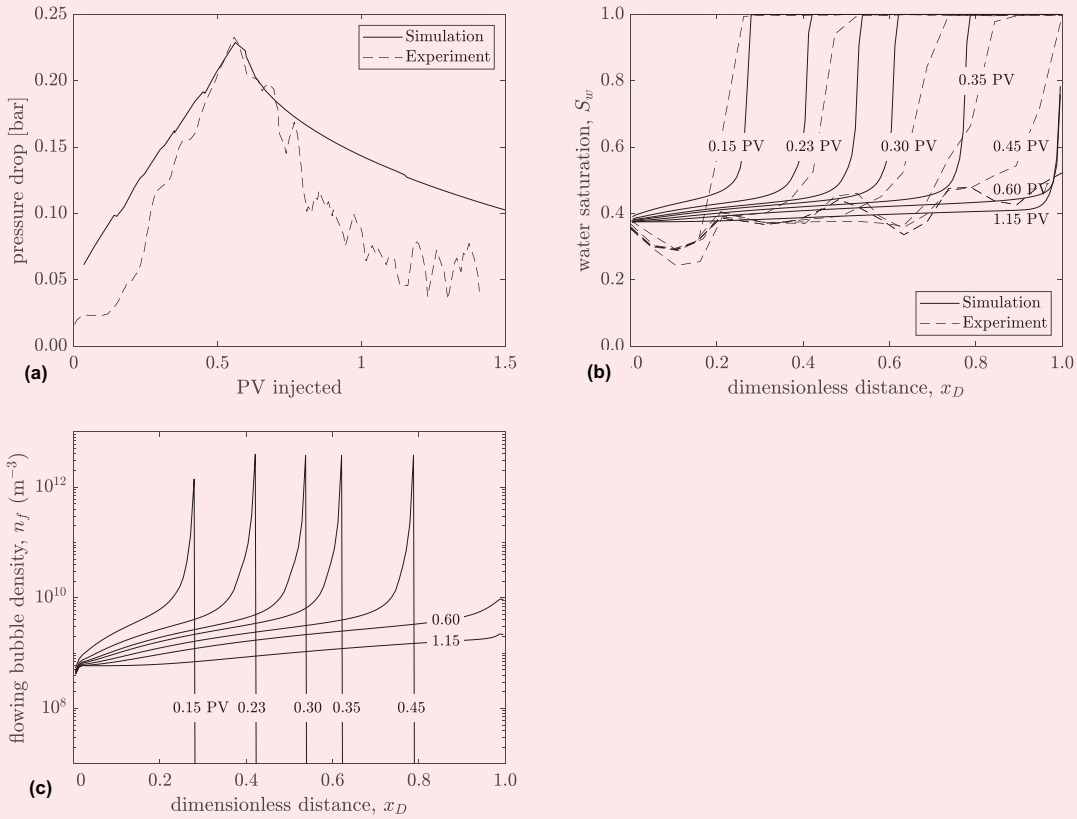

Table 2 *The multiphase and foam parameters used in the local equilibrium model.*

Multiphase Parameters	
k^0_{rw}	0.75
k^0_{rg}	1.0
S_{rw}	0.2
S_{rg}	0.0
μ_w (Pa-sec)	1.0×10^{-3}
μ_g (Pa-sec)	2.3×10^{-5}
Foam Parameters	
α (Pa sec$^{2/3}$ m$^{10/3}$)	9.2×10^{-16}
k_1 (sec$^{1/3}$ m$^{-13/3}$)	8.6×10^{13}
k_{-1} (m^{-1})	17
n^*_f (m^{-3})	4.0×10^{12}
X_t^{max} max	0.8
P_c^* (Pa)	3.5×10^{4}

as determined by the combination of the parameters used to predict the flow behavior.

Another small discrepancy between the model and the experiments is seen in the propagation velocity of the front. The model fronts seem to be moving faster initially but slows down significantly as the pressure drop is increased. By examining the model's output of the pressure drop, we notice that the numerical pressure drop is larger than the experimental one. This could be why we observe the slowdown in the frontal displacement velocity. Overall, we believe that the model decently matches the complex experimental data.

To complement the analysis, we plotted the bubble density profiles corresponding to the various times where the saturation profiles where acquired, Fig. 2c. The bubble density increases significantly from the inlet to the front where it reaches a maximum value. Most generation occurs at the front where the bubble density is at its maximum; however, as the water saturation decreases and the capillary pressure approaches that of the limiting capillary pressure of the foam in question, the bubble density settles down to an equilibrium value. The equilibrium value is when generation events cancel out coalescence events. Much later in the displacement at 1.15 pore volume injected, we can see that the foam is

starting to weaken as the bubble density is decreasing, indicating that the bubbles' sizes are increasing.

Another important behavior to examine after building any foam parameter is the steady-state behavior that the model outputs. Osterloh and Jante (1992)[27] measured the steady-state pressure drop values at various combinations of water and gas velocities. Upon plotting their results, they discovered that there are two regimes that are observed in steady-state foam flow[27].

The first regime is the low quality regime, where the water velocity is much larger than the gas velocity. In this regime, they observed that the pressure drop is independent of the water velocity and is dependent on the gas velocity. The second regime is termed the high quality regime, where the gas velocity is much larger than the water velocity. In that regime, the pressure drop changed with changing water velocity, but remained unchanged with changing gas velocity.

Figure 3a plots the pressure drop contour output using the parameters listed in Table 2. We can clearly see that there are two distinct regimes: the low quality regime and the high quality regime, as indicated experimentally in the literature. The transition between the two regimes is smooth and there are no kinks indicating that the model is working transitioning smoothly between regimes.

The final plot we examine is what is termed the foam scan plot. In a foam scan plot, the total velocity is fixed while the foam quality is altered. Typically, the pressure drop increases until a certain value (f_g^*), which is called the transition foam quality[28]. The transition foam quality represents the foam quality above which the foam enters the high quality regime. The transition quality depends on the surfactants used, the type of rock used, the ions in the water, and fluid/rock interactions. A foam that has a large transition quality is preferred because it uses less water — and therefore less surfactant — to reach larger pressure drops. Figure 3b shows our model's output. Generally, it captures what we expect in a foam scan plot.

Fig. 3 *Pressure drop estimates of the model presented into the two commonly reported plots. (a) The pressure drop contours in bars are plotted as a function of aqueous and gaseous phase velocities, and (b) a foam scan is performed at various total injection velocities.*

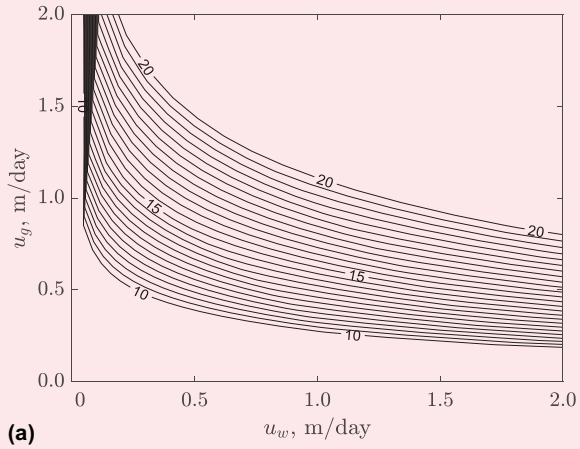

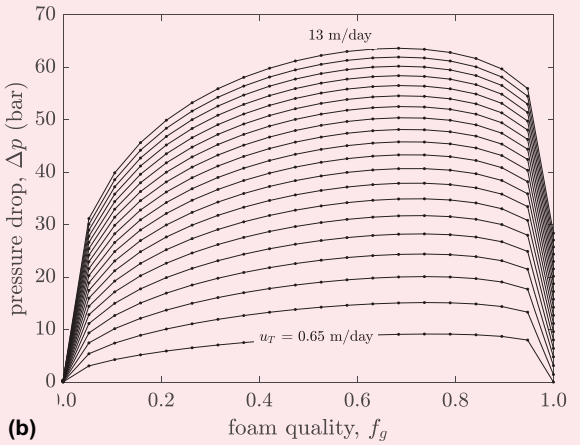

Conclusions

We have implemented a local equilibrium model that is able to predict foam flow in porous media. The essence of the model is that it assumes that the time of reaction (generation or coalescence) is much faster than the time of transport processes (flow), therefore, instantaneous equilibrium is reached as soon as gas and water (with surfactant) occupies any space.

The local equilibrium model maintains the main mechanisms that constitute the full-physics population balance model but obtains faster solutions. This, in turn, makes the local equilibrium model suitable and competitive with current used simulators for simulation of foam in the field case applications. Because foam flow is significantly affected by how much gas is trapped/flowing, we also adopted a new flowing foam fraction that takes account of the X_f dependence on the pressure gradient, the permeability, and the apparent viscosity — because of the dependence on the total velocity.

The developed model was implemented in the open-source MRST to demonstrate its effectiveness and ease of implementation. We compared the model results with CO_2 foam experimental results that were done on sandstones. The model matched the experimental results satisfactorily. Moreover, the model was shown to be capable of producing common foam plots that are used in assessing foam behavior in porous media: foam quality scan plot, and the pressure drop contours plot. Both of these plots gave the expected behavior.

Finally, although the model showed promising results, there are improvements and further developments that need to be added to it. The transient surfactant flow was not implemented and should be coupled with the current model. Additionally, the dependency of any of the parameters on the local surfactant concentrations is another area of improvement. Although, the effect of the surfactant structure (or mixture of surfactants) is not implemented in the current model, but remains an area of research for future developments.

References

1. Lake, L.W., Johns, R., Rossen, W.R. and Pope, G.A.: *Fundamentals of Enhanced Oil Recovery,* SPE, Richardson, Texas, 2014, 496 p.
2. Orr Jr., F.M.: *Theory of Gas Injection Processes*, Tie-Line Publications, Holte, Denmark, 2007, 381 p.
3. Almajid, M.M., Nazari, N. and Kovscek, A.R.: "Modeling Steady-State Foam Flow: Hysteresis and Backward Front Movement," *Energy and Fuels*, Vol. 33, Issue 11, 2019, pp. 11353-11363.
4. Almajid, M.M. and Kovscek, A.R.: "Pore Level Mechanics of Foam Generation and Coalescence in the Presence of Oil," *Advances in Colloid and Interface Science*, Vol. 233, July 2016, pp. 65-82.
5. Radke, C.J. and Gillis, J.V.: "Dual Gas Tracer Technique for Determining Trapped Gas Saturation during Steady Foam Flow in Porous Media," SPE paper 20519, presented at the SPE Annual Technical Conference and Exhibition, New Orleans, Louisiana, September 23-26, 1990.
6. Hirasaki, G.J. and Lawson, J.B.: "Mechanisms of Foam Flow in Porous Media: Apparent Viscosity in Smooth Capillaries," *SPE Journal*, Vol. 25, Issue 2, April 1985, pp. 176-190.
7. Tang, G-Q. and Kovscek, A.R.: "Trapped Gas Fraction during Steady-State Foam Flow," *Transport in Porous Media*, Vol. 65, 2006, pp. 287-307.
8. Ma, K., Ren, G., Mateen, K., Morel, D., et al.: "Modeling Techniques for Foam Flow in Porous Media," *SPE Journal*, Vol. 20, Issue 3, June 2015, pp. 453-470.
9. Almajid, M.M. and Kovscek, A.R.: "Pore Network Investigation of Trapped Gas and Foam Generation Mechanisms," *Transport in Porous Media*, Vol. 131, Issue 11, January 2020, pp. 1-25.
10. Kharabaf, H. and Yortsos, Y.C.: "Invasion Percolation with Memory," *Physical Review E*, Vol. 55, Issue 6, June 1997, pp. 739-751.
11. Chen, Q., Gerritsen, M.G. and Kovscek, A.R.: "Modeling Foam Displacement with the Local Equilibrium Approximation: Theory and Experimental Verification," *SPE Journal*, Vol. 15, Issue 1, March 2010, pp. 171-183.
12. Cheng, L., Reme, A.B., Shan, D., Coombe, D.A., et al.: "Simulating Foam Processes at High and Low Foam Qualities," SPE paper 59287, presented at the SPE/DOE Improved Oil Recovery Symposium, Tulsa, Oklahoma, April 3-5, 2000.
13. Kharabaf, H. and Yortsos, Y.C.: "Pore Network Model for Foam Formation and Propagation in Porous Media," SPE paper 36663, presented at the SPE Annual Technical Conference and Exhibition, Denver, Colorado, October 7-9, 1996.
14. Khatib, Z.I., Hirasaki, G.J. and Falls, A.H.: "Effects of Capillary Pressure on Coalescence and Phase Mobilities in Foams Flowing through Porous Media," *SPE Reservoir Engineering*, Vol. 3, Issue 3, August 1988, pp. 919-926.
15. Aronson, A.S., Bergeron, V., Fagan, M.E. and Radke, C.J.: "The Influence of Disjoining Pressure on Foam Stability and Flow in Porous Media," *Colloids and Surfaces A: Physicochemical and Engineering Aspects*, Vol. 83, Issue 2, March 1994, pp. 109-120.
16. Jiménez, A.I. and Radke, C.J.: "Dynamic Stability of a Foam Lamellae Flowing through a Periodically Constricted Pore," Chapter 25 in *Oil Field Chemistry: Enhanced Recovery and Production Stimulation*, ACS Symposium Series, Vol. 396, 1989, pp. 460-479.
17. Kovscek, A R., Tang, G-Q. and Radke, C.J.: "Verification of Roof Snap-Off as a Foam Generation Mechanism in Porous Media at Steady-State," *Colloids and Surfaces A: Physicochemical and Engineering Aspects*, Vol. 302, Issues 1-3, July 2007, pp. 251-260.
18. Kahrobaei, S. and Farajzadeh, R.: "Insights into Effects of Surfactant Concentration on Foam Behavior in Porous Media," *Energy & Fuels*, Vol. 33, Issue 2, January 2019, pp. 822-829.
19. Kovscek, A.R., Patzek, T.W. and Radke, C.J.: "A Mechanistic Population Balance Model for Transient and Steady-State Foam Flow in Boise Sandstone," *Chemical Engineering Science*, Vol. 50, Issue 23, December 1995, pp. 3783-3799.
20. Balan, H.O., Balhoff, M.T., Nguyen, Q.P. and Rossen, W.R.: "Network Modeling of Gas Trapping and Mobility in Foam Enhanced Oil Recovery," *Energy & Fuels*, Vol. 25, Issue 9, August 2011, pp. 3974-3987.
21. Luo, H., Ma, K., Mateen, K., Ren, G., et al.: "A Mechanistic Foam Simulator Incorporating Systematic Dependencies of Various Foam Properties on Permeability," SPE paper 193868, presented at the SPE Reservoir Simulation Conference, Galveston, Texas, April 10-11, 2019.
22. Kovscek, A.R. and Bertin, H.J.: "Foam Mobility in Heterogeneous Porous Media," *Transport in Porous Media*, Vol. 52, 2003, pp. 17-35.
23. Friedmann, F., Chen, W.H. and Gauglitz, P.A.: "Experimental and Simulation Study of High Temperature Foam Displacement in Porous Media," *SPE Reservoir Engineering*, Vol. 6, Issue 1, February 1991, pp. 37-45.
24. Ettinger, R.A. and Radke, C.J.: "The Influence of Texture on Steady Foam Flow in Berea Sandstone," *SPE Reservoir Engineering*, Vol. 7, Issue 1, February 1992, pp. 83-90.
25. Chen, Q.: "Assessing and Improving Steam-Assisted Gravity Drainage: Reservoir Heterogeneities, Hydraulic Fractures, and Mobility Control Foams," Ph.D. thesis, Stanford University, May 2009, 197 p.
26. Farajzadeh, R., Andrianov, A., Bruining, H. and Zitha, P.L.J.: "Comparative Study of CO_2 and N_2 Foams in Porous Media at Low and High Pressure Temperatures," *Industrial & Engineering Chemistry Research*, Vol. 48, Issue 9, April 2009, pp. 4542-4552.
27. Osterloh, W.T. and Jante Jr., M.J.: "Effects of Gas and Liquid Velocity on Steady-State Foam Flow at High Temperature," SPE paper 24179, presented at the SPE/DOE Enhanced Oil Recovery Symposium, Tulsa, Oklahoma, April 22-24, 1992.
28. Alvarez, J.M., Rivas, H.J. and Rossen, W.R.: "Unified Model for Steady-State Foam Behavior at High and Low Foam Qualities," *SPE Journal*, Vol. 6, Issue 3, September 2001, pp. 325-333.

About the Authors

Dr. Muhammad M. Almajid

Ph.D. in Petroleum Engineering, Stanford University

Dr. Muhammad M. Almajid joined Saudi Aramco as a Petroleum Engineer in 2006. He is currently working in the Reservoir Engineering Technology Division of Saudi Aramco's Exploration and Petroleum Engineering Center – Advanced Research Center (EXPEC ARC). Muhammad's main research is focused on carbon dioxide (CO_2) flow in porous media, including enhanced oil recovery (EOR) and sequestration. He is currently co-leading the CO_2 sequestration, the gravity override, and the gas mobility control research. Muhammad is also part of the team working on the CO_2 EOR pilot.

He has authored and coauthored numerous technical papers, and filed several patent applications.

In 2011, Muhammad received his B.S. degree in Petroleum Engineering from the Colorado School of Mines, Golden, CO. In 2015, he received his M.S. degree, and in 2019 his Ph.D. degree, both in Petroleum Engineering from Stanford University, Stanford, CA.

Dr. Zuhair A. Al-Yousif

Ph.D. in Petroleum Engineering, Texas A&M University

Dr. Zuhair A. Al-Yousif joined Saudi Aramco as a Petroleum Engineer in 2008. He is currently working in the Reservoir Engineering Technology Division of Saudi Aramco's Exploration and Petroleum Engineering Center – Advanced Research Center (EXPEC ARC). The emphasis of his work has been on enhanced oil recovery (EOR).

Zuhair is currently co-leading the gravity override mitigation, the gas mobility control and carbon dioxide (CO_2) sequestration research, and contributing to high impact projects within the area of CO_2 EOR.

He has authored and coauthored numerous technical papers, and filed several patent applications.

Zuhair has been appointed to serve as an Associate Editor in the editorial board of the *Journal of Petroleum Science and Engineering* and the *Journal of Petroleum Exploration and Production Technology*.

In 2008, he received his B.S. degree from King Fahd University of Petroleum and Minerals (KFUPM), Dhahran, Saudi Arabia. In 2012, he received his M.S. degree, and in 2017 his Ph.D. degree, both in Petroleum Engineering from Texas A&M University, College Station, TX.

Othman S. Swaie

B.S. in Business Administration, Arab Open University

Othman S. Swaie joined Saudi Aramco as a Laboratory Technician in 2010. He is currently working in the Reservoir Engineering Technology Division of Saudi Aramco's Exploration and Petroleum Engineering Center – Advanced Research Center (EXPEC ARC). Prior to this, he worked at SABIC from 2006 to 2010 as a Laboratory Technician. At the beginning of his career with Saudi Aramco, Othman worked in the Southern Area Laboratory Division (Abqaiq Lab) in the Analytical Support Unit where he worked until mid-2017.

Othman is currently working in the carbon dioxide enhanced oil recovery focus area.

In 2006, he received a diploma in Industrial Laboratory Technology from Jubail Industrial College, Jubail, Saudi Arabia. In 2012, Othman received his B.S. degree in Business Administration from Arab Open University, Dammam, Saudi Arabia.

The Measurement of Tortuosity of Porous Media Using Imaging, Electrical Measurements, and Pulsed Field Gradient NMR

Dr. Hyung T. Kwak, Mahmoud Elsayed, Dr. Ammar El-Husseiny and Dr. Mohamed A. Mahmoud

Abstract /

Tortuosity, in general, characterizes the geometric complexity of porous media. It is considered as one of the key factors in characterizing the heterogeneous structure of porous media and has significant implications for macroscopic transport flow properties. There are four widely used definitions of tortuosity that are relevant to different fields from hydrology to chemical and petroleum engineering, which are: geometric, hydraulic, electrical, and diffusional.

Recent work showed that hydraulic, electrical, and diffusional tortuosity values are roughly equal to each other in glass beads. Nevertheless, the relationship between the different definitions of tortuosity in natural rocks is not well understood yet. Understanding the relationship between the different tortuosity definitions in rocks can help to establish a workflow that allows us to estimate other types from the available technique. Therefore, the objective of this study is to investigate the relationship between the different tortuosity definitions in natural rocks.

A major focus of this work is to utilize nuclear magnetic resonance (NMR) technology to estimate tortuosity. Such a technique has been traditionally used to obtain diffusional tortuosity, which can be defined as the ratio of the free fluid self-diffusion coefficient to the restricted fluid self-diffusion coefficient inside the porous media.

In this study, the following techniques were used to quantify hydraulic, electrical, and diffusional tortuosity, respectively, on the same rock sample: (1) Micro-computed tomography (micro-CT) 3D imaging, (2) four electrode resistivity measurements, and (3) pulsed field gradient NMR (PFG NMR). PFG NMR is a very powerful, noninvasive technique employed to measure the self-diffusion coefficient for free and confined fluids. The measurements were done based on two carbonate rock core plugs characterized by variable porosity, permeability, and texture complexity.

Results show that PFG NMR can be applied directionally to quantify the pore network anisotropy created by fractures. For both samples, hydraulic tortuosity was found to have the lowest magnitude compared to geometric, electrical, and diffusional tortuosity. This could be explained by the more heterogeneous microstructure of carbonate rocks. The NMR technique has advantages over the other electrical and imaging techniques for tortuosity characterization: it is faster, nondestructive, and can be applied in a wellbore environment (in situ).

We therefore conclude that NMR can used as a tool for estimating not only diffusional tortuosity but also for indirectly obtaining hydraulic and electrical tortuosity.

Introduction

Rock tortuosity is defined as the ratio of the fluid flow pathway to the straight-line distance between the two ends of the rock. It describes the geometry of flow paths, which is a measure of the heterogeneity and complexity of the rock. It is an important parameter to quantify the transport behavior of fluid flow in porous media, therefore, accurate measurements of heterogeneous microstructure is required[1, 2]. Tortuosity has been widely used in several scientific and engineering fields such as geoscience[3, 4], energy storage and conversion[5, 6], water treatment[7], and in bone tissue engineering[8, 9].

Due to the wide range of applications, scientists and engineers are using different definitions for tortuosity interchangeably, including geometric, hydraulic, electrical, and diffusion tortuosity[10]. The tortuosity types are controlled by the experimental methodology utilized to estimate them.

Geometric Tortuosity

Geometric tortuosity describes the effective path length of the pores in the porous medium to the direct length[11]. Geometric tortuosity, τ_g, is the ratio of the average length, L, of the geometric paths inside the porous medium to the straight-line length, L_o, across the porous medium, Eqn. 1:

$$\tau_g = \frac{L}{L_o} \quad (1)$$

It is usually computed through imaging techniques such as X-ray micro-computed tomography (micro-CT)[12] and focused ion beam and scanning electron microscopy (FIB-SEM)[13] by evaluating the shortest fluid pathways as the actual fluid flow in porous media[14]. There are several evaluation methods to estimate the shortest fluid pathways in porous rocks such as the direct shortest path searching method[15], the skeleton shortest path searching method[16], the fast marching method[17], and the pore centroid method[18].

Geometric tortuosity usually does not estimate/predict the dynamic properties of porous media such as permeability, conductivity, and diffusion because it ignores the flow dynamics in the cross section of the pore channels and it only highlights the longitudinal distance of possible flow paths[10]. Subsequently, it is important to estimate the constriction features and dead-end pore channels that significantly affect the fluid flow in porous media.

Hydraulic Tortuosity

Hydraulic tortuosity measures the restriction to fluid flow imposed by the porous matrix. It first appeared as a factor in the Kozeny-Carman equation to account for the reduction in permeability caused by the sinuous nature of the flow channels[19]. Like geometric tortuosity, it is defined as the ratio of actual to straight-line lengths between points in a porous medium, however, it is a more refined definition since it accounts for curved streamlines and viscous effects at pore walls[19, 20].

Berg (2014)[21] showed that by using the Kozeny-Carman equation that porosity and permeability can be related through pore structure parameters such as characteristic length, tortuosity, and constriction. The principle is extended to idealized pore materials, in which Darcy's fluid flow law from the Hagen-Poiseuille equation is reproduced. Several 3D pore network models were constructed for Fontainebleau sandstone to compare the hydraulic tortuosity using micro-CT data and the constructed idealized model.

The Kozeny-Carman equation is derived and subsequently rearranged into the form used for hydraulic tortuosity predictions. The derivation has been adapted from Wylie and Spangler (1952)[22]. The Hagen-Poiseuille equation, Eqn. 2, describing capillary flow is given as:

$$u_e = \frac{d^2}{32}\frac{\Delta P}{\mu L_e} \quad (2)$$

where, u_e is the interstitial velocity, d is the channel diameter, ΔP is the pressure driving force across the capillary, μ is the viscosity, and L_e is the channel length.

Now, for porous media, i.e., capillaries with a noncircular cross section, $\frac{d^2}{32}$ is replaced by $\frac{m^2}{\beta}$, where β is a shape factor correction and m is an equivalent hydraulic diameter given by Eqn. 3, where $\left(\frac{S}{V}\right)$ is the surface area per unit volume ratio of the porous medium.

$$m = \frac{\phi}{\left(\frac{S}{V}\right)} \quad (3)$$

For porous media, if the seepage velocity, u, is constant, then the interstitial velocity, u_e, through the channels of the matrix must be increased to account for the reduced cross-sectional area and increased length that the fluids are traveling. Therefore, the relationship between the u and the u_e is given by Eqn. 4[19].

$$u_e = \frac{u}{\phi}\left(\frac{L_e}{L}\right) \quad (4)$$

Substituting Eqn. 5 into Eqn. 2 and solving for u yields:

$$u = \frac{m^2\phi}{\beta}\left(\frac{L}{L_e}\right)^2\frac{\Delta P}{\mu L} \quad (5)$$

Equation 6 is analogous to Darcy's equation, given by:

$$u = k\frac{\Delta P}{\mu L} \quad (6)$$

Comparing Eqns. 5 and 6; the permeability, k, in Eqn. 6 is equivalent to $\frac{m^2\phi}{\beta\left(\frac{L_e}{L}\right)^2}$. Substituting in m from Eqn. 3 and equating these two terms yields the Kozeny-Carman relationship, Eqn. 7:

$$k = \frac{\phi^3}{\beta\left(\frac{L_e}{L}\right)^2\left(\frac{S}{V}\right)^2} \quad (7)$$

The term $\left(\frac{L_e}{L}\right)^2$ is equal to hydraulic tortuosity (τ_H). Rearranging Eqn. 7 for τ_H yields:

$$\tau_H = \sqrt{\frac{\phi^3}{k\beta\left(\frac{S}{V}\right)^2}} \quad (8)$$

Equation 8 is the rearranged form of the Kozeny-Carman equation that will be used to estimate hydraulic tortuosity. Subsequently, the flow flux differs continuously across the flow direction influenced by its cross-section, shape, inclination, branching and joining, which complicates the recognition of pore scale flow streamlines.

Electrical Tortuosity

The electrical resistivity of a sedimentary rock saturated with brine is an essential element in the interpretation of electric resistivity logs in petroleum exploration. The significance of the connections between a pore microstructure and the electrical resistivity of the rock has resulted in significant studies without producing an adequate theoretical definition[23]. The electrical resistivity of sedimentary rocks saturated with brine depends on electrical resistivity of the fluid, porosity of the rock, and the pore microstructure relative to the applied electrical voltage.

There are several factors affecting the electrical resistivity of sedimentary rocks such as water saturation; temperature, brine saturation, ions types and strength of the salt in the brine solution; and cation exchange capacity between rock and brine. As a consequence, high frequency electrical conductance measurements were exploited to screen underground movement of reservoir fluids, rock integrity testing, and leakage detection[24]. The formation resistivity factor is a terminology used to relate the electrical resistivity of the rock saturated with brine, R_o, and the resistivity of the brine, R_w, Eqn. 9:

$$F = \frac{R_o}{R_w} \quad (9)$$

The relative effect of the ions added by cation exchange becomes small as the salinity of the brine in the pores increases. Measuring resistivity with a high salinity brine saturating rock usually reaches the expected constant formation factor in the absence of clays. When water comes into contact with these clays in the rock, many phenomena can occur. The clay swells to several times their original size under low salinity brine saturating the rock, which increases the viscosity of the clay-water blend and reduces the cross section for current conduction[25].

To describe the conductivity of a porous medium, Archie (1942)[26] developed an empirical relationship between the formation resistivity factor and the porosity. Equation 10 describes this relationship:

$$F = a\,\varphi^{-m} \tag{10}$$

where a is a structural parameter and m is the cementation exponent, which has different values for different lithologies. Both of these parameters are useful for pore characterization, which can be correlated to different textural rock properties[27].

In general, higher values of the cementation factor corresponds to a higher value of tortuosity[28]. Electrical tortuosity has a significant impact on different petrophysical parameters such as permeability, surface to volume ratio, resistivity of the brine, clay minerals content, rock porosity, and rock resistivity[28]. In addition, the type of porosity in the porous medium plays an important role in the variation of tortuosity. Some of the factors that contribute to increase the electrical tortuosity include:

- Dead-end pores, which are usually part of the microporosity of the rocks and can result in complicating the current to be flown through the pores.
- Rock samples with matrix of highly heterogeneous structure causes more resistance to the electrical current.
- The rocks, defined by the complexity of the electrolytic routes, are more resistant when they pass through the pore.

Cornell and Katz (1953)[29] suggested a correlation to estimate the electrical tortuosity, which is a simplified form from Archie's equation. The parameter, a, in Eqn. 10 is function of tortuosity, τ_e, which is a term corresponding to the path length of the electrical current or the way the pores are interconnected.

Figure 1 shows the equivalent electrical circuit of a porous rock sample. The r_{matrix} and r_w are the resistances of the rock matrix and brine filling the porous space, respectively. The overall resistance of the rock, r_o, can be expressed in terms of the r_{matrix} and r_w, which are in parallel. To derive the equation of parallel resistors, we should start from Ohm's law showing that the current, i, spilt with a constant potential difference, across the core as follows:

$$i = \frac{V}{r} \tag{11}$$

$$i = i_1 + i_2 \tag{12}$$

Fig. 1 *The equivalent electrical circuit of a porous rock sample.*

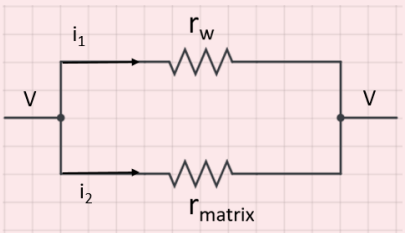

$$\frac{V}{r_o} = \frac{V}{r_w} + \frac{V}{r_{matrix}} \tag{13}$$

$$V\left(\frac{1}{r_o}\right) = V\left(\frac{1}{r_w} + \frac{1}{r_{matrix}}\right) \tag{14}$$

$$\frac{1}{r_o} = \frac{1}{r_w} + \frac{1}{r_{matrix}} \tag{15}$$

In case we consider that the rock sample is made up of a very resistive matrix (nonconductive material), $r_{matrix} = \infty$, the previous equation can be reduced to:

$$r_o = r_w \tag{16}$$

The ions' movement inside the porous media is directed to a tortuous path, so the length of the equivalent water volume, L_e, is greater than the actual path, L, and then the volume of water in the porous media is $AL\varphi$. The cross-sectional area of equivalent water volume, A_e, is $AL\varphi/L_e$.

$$r_o = R_o\left(\frac{L}{A}\right) \tag{17}$$

$$r_w = R_w\left(\frac{L_e}{A_e}\right) = R_w\left(\frac{L_e^2}{AL\varphi}\right) \tag{18}$$

Because $r_o = r_w$, and

$$R_o\left(\frac{L}{A}\right) = R_w\left(\frac{L_e^2}{AL\varphi}\right) \tag{19}$$

$$F = \frac{R_o}{R_w} \tag{20}$$

$$F = \left(\frac{L_e}{L}\right)^2 \frac{1}{\varphi} = \frac{\tau_e^2}{\varphi} \tag{21}$$

$$\tau_e^2 = F\,\varphi \tag{22}$$

$$\tau_e = \sqrt{F\varphi} \tag{23}$$

Pores are not equal in the electrical flow of the rock, and are regarded as traps and channels based on their current permissible flow[30]. Therefore, for the interpretation of the electric measurement results, it is desirable to understand the pore geometry described by type, shape, and interconnectedness of the porous medium. In reservoir rocks, pore throats are the paths for electrical current flow, and the large pore throats lead to lower resistivity while the small pore throats complicate the current flow, which results in higher resistivity[27].

The electrical tortuosity for carbonate rock study results in several correlations between tortuosity and some other petrophysical properties[27]. Tortuosity correlations showed an increasing tortuosity with decreasing porosity, permeability, Archie cementation factor, and increasing with resistivity formation factor.

Saner et al. (1996)[27] found that the mean electrical tortuosity values for granular and dolomitic-muddy is 2, where the former has an average value of 1.9, and the latter showed an average value of 2.3, using Eqn. 23.

Diffusion Tortuosity

Because of the pore geometry restrictions, the molecules that diffuse within the porous space will be expected to have a diffusion coefficient different from that of the bulk fluid[31]. Therefore, it is thought that restricted diffusion research can result in information leading to characterization of the pore structure. We propose the utilization of the pulsed field gradient nuclear magnetic resonance (PFG NMR) technique to study free and restricted diffusion of a probing fluid in porous media. Using very low diffusion time gives an indication in evaluating the surface to volume ratio, and it is called the short time regime. On the other, using sufficiently large diffusion time gives the diffusion tortuosity value and it is known as the long-time regime[32].

It is a truly challenging task to measure diffusion or mean square displacement due to Brownian motion in heterogeneous media by PFG NMR. The presence of a term for surface relaxation implies that the NMR experiments may not represent the actual geometry. Furthermore, internal magnetic field gradients can considerably affect diffusion measurements[33-35].

The tortuosity is an important parameter that characterizes the interconnectedness of the pore space. Diffusive tortuosity, τ_d, is defined as the diffusing coefficient of particles in the free fluid, D, relative to its diffusion in the porous medium, D_R[36]. It can be expressed mathematically as:

$$\tau_d = \frac{D}{D_R} \qquad 24$$

Consequently, measuring the diffusion tortuosity using PFG NMR is not always readily achievable because the experiment is limited by the lifetime of the NMR signal. For example, the lifetime of the water signal may be so long that the length scales up to 100 µm can be examined in porous rock saturated with water. Previous publications have used noble gases to avoid this issue due to its higher diffusion coefficient, which will result in probing the heterogeneity of the porous medium in less time[37-39].

These measurements confirm that the tortuosity limit (asymptotic value) has been reached for the diffusion coefficient as restricted diffusion is no longer dependent on observation time. The PFG NMR experiment sometimes could be used under these circumstances to test length scales of the order of millimeters. Mair et al. (1999)[37] stated that gas diffusion NMR can measure the pore space surface area to volume ratio and the tortuosity accurately. The authors also noted that gas diffusion NMR provides a good measure of the tortuosity of sandstone and heterogeneous carbonate rocks.

NMR restricted diffusion measurements of liquid imbibed in porous media detects the rock structure on length scales greater than 50 µm. Using such a system will allow us to measure the porosity and pore surface area to volume ratio (S/V_p) accurately. Although, this method did not recognize the interconnectedness and tortuosity of the complex pore systems such as sedimentary rocks using the simple PFG NMR[38].

The tortuosity values of various sandstones from geothermal wells in Germany were measured based on a restricted diffusion coefficient that was confirmed to be independent of time[40]. These measurements correlated strongly with the tortuosity obtained from various other techniques, including electrical and petrographical imaging[40]. Another study[39] performed a tortuosity experiment on different rock samples using NMR of laser polarized gas. Fontainebleau sandstone showed a tortuosity value of 3.45, which is approximately equal to the value obtained in Hurlimann et al. (1994)[35].

An additional three carbonate samples (Edwards limestone, Austin chalk, and Indiana limestone) were studied to measure the diffusion tortuosity, and the results showed an increase in tortuosity values with the decrease of permeability. The tortuosity values range between 4.76 to 7.69, and the Indiana limestone also showed very close tortuosity value, 7.69, to the one studied in Hurlimann et al. (1994)[35].

A recent study that was performed in carbonate plugs using methane as the diffused fluid inside the porous media showed that electrical tortuosity correlates linearly with diffusion tortuosity measured using PFG NMR[41].

PFG NMR

The PFG NMR techniques are used to study the motion of the molecules without interfering with the body under study, therefore, it is a very powerful method to measure τ_d, as defined in Eqn. 24[35, 42]. The PFG NMR techniques have been successfully applied to many systems for studying diffusion in bulk liquids, solids, and fluids in restricted geometries, as well as in emulsions[36, 43]. The significance of the PFG experiment is that the Fourier transformation of the fluid diffusion propagator in the pore space is measured directly[32]. In sedimentary rock, the pore boundaries limit fluid molecules' self-diffusion. Therefore, in geometrically restricted structures, the measurement of molecular diffusivity is lower than in bulk fluid. Subsequently, it is believed that restricted diffusion can assist in obtaining direct information to estimate the pore structure characterization.

In the PFG NMR diffusion measurements, usually two gradient pulses are applied. The two gradients serve to detect the effect of relative movements of the nuclei during an experimental diffusion time. The spatial positions of individual nuclei are identified by the phase of each spin. The first gradient pulse de-phases the spins such that the phases of these spins depend on the spin location and are proportional to γgr. The second gradient pulse, is applied after a time rephases the spins for

observation. During the diffusion time, Δ, is the relative distance for which each spin has diffused away from its original position. As long as the actual mean diffusion distance does not exceed the entire sample dimension, the measured diffusivity is independent. In contrast, for geometrically restricted systems, the actual diffusion length is confined by the boundaries.

It turns out, however, that restricted diffusion measured in this way may, in addition to purely geometric properties of the medium, also be influenced by surface interactions. Contributions of the surface interaction to restricted diffusion, and therefore, to τ_e, can be traced by either varying the fluid or by surface modification of the porous solid under study.

Moreover, careful experimental design is needed to remain careful because of the internal magnetic field gradients, which result from susceptibility differences between r_{matrix} and pore fluid[44]. Measuring the bulk fluid self-diffusion coefficient, D, by the NMR PFG technique was first studied by Stejskal and Tanner (1965)[45]. The technique basically depends on the NMR signal, S, attenuation due to molecular diffusion between two pulsed gradients of the magnetic field. Normalization of the S intensity to the signal intensity without applied field gradients, S_0, cancels out any effects of signal attenuation due to relaxation.

$$\frac{S}{S_0} = \exp\left(-D(\gamma g\delta)^2\left(\Delta - \frac{\delta}{3}\right)\right) = \exp(-bD) \qquad 25$$

where D = self-diffusion coefficient of the fluid (m^2/s). S_0 = NMR signal in the absence of applied magnetic field gradients (μV), Δ = duration between two applied magnetic field "diffusion time" (msec), δ = duration of the applied magnetic field gradient (msec), g = strength of the applied magnetic field gradient (T/m), and γ = gyromagnetic ratio of the nucleus being studied (= 2.68 × 108 Hz/T for 1H nucleus).

These techniques of diffusion NMR take advantage of the spatial variation in the Larmor frequency when a gradient is applied to encode the position of the molecule for diffusion measurement[46]. Their pulse sequences, Fig. 2, consist of RF pulses, gradient pulses with strength, g, and a diffusion time, Δ, for which the molecules' diffusion is measured and the duration δ that flip and unflip the magnetization, which is used to label the molecules' position through its spin.

While the separation of the RF pulses, and the RF pulse and the signal acquisition are a delay in the PFG spin echo (PFGSE), the PFG stimulated spin echo (PGSTE) enables the periods of spin-spin relaxation, T_2 relaxation, to be minimized. The magnetization in the PGSTE is stored along the longitudinal axis during the diffusion time and spin-lattice relaxation, T_1 relaxation, is used to help prevent signal loss from T_2 alone enabling longer diffusion times to be probed[48].

When diffusion occurs during Δ, it is described as a dephasing of the spins and the attenuation in the NMR signal is obtained. Plotting signal attenuation (S/S_0) against the g is used to calculate the diffusion coefficient since all other parameters are fixed for each experiment.

Fig. 2 *(a) The PFGSE sequence, and (b) the PGSTE sequence used in the bulk fluid diffusion experiment[47].*

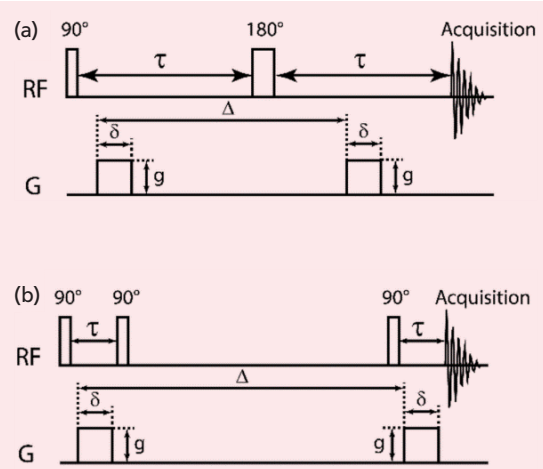

Usually in practice, linear fit is obtained by plotting the natural log of the S/S_0 vs. a parameter b shown in Eqn. 25, which combines all of the fixed parameters with a gradient term. This simplifies the result analysis since the slope will directly be the diffusion coefficient.

The magnetic susceptibility difference between the r_{matrix} and the pore fluid results in an internal magnetic field gradient, which can cause an excessive S/S_0 for the PFG NMR experiment. Another pulse sequence is required to decrease the systematic error in the measurements since sometimes this internal magnetic field g becomes greater than the applied. The 13-interval bipolar gradients pulse sequence (BG-PFGSTE) is used for cases of high magnetic susceptibility difference to avoid excessive S/S_0[49]. A schematic of this sequence is shown in Fig. 3[50]: This pulse sequence is a stimulated echo sequence with two refocusing 180° RF pulses to prepare molecules for the diffusion time and read intervals for signal acquisition[51].

The accumulation of the phase encoding caused by

Fig. 3 *A schematic of the 13-interval BG-PFGSTE used in the restricted diffusion experiments in the rock cores[50].*

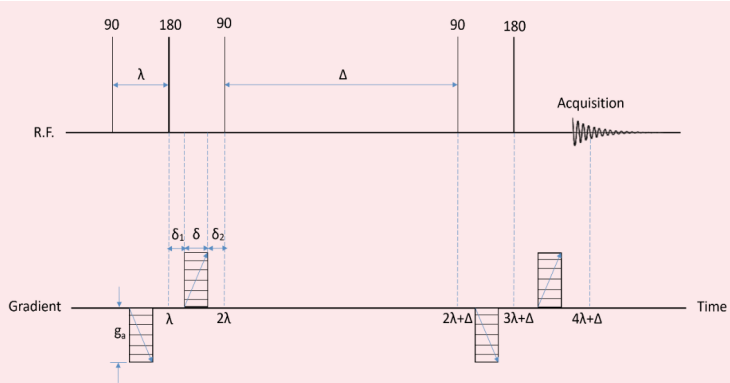

the applied gradients is exploited to reduce the effects of internal field gradients on the echo amplitude by using 180° refocusing pulses and oppositely polarized applied field gradients. Also, the effect of an internal gradient is eliminated by refocusing constantly the polarized internal magnetic field gradient, which occurred by the phase encoding[52]. In the case of applied magnetics field gradients, the influence of the internal gradient is dominating the signal attenuation, which can be homogeneous with the applied gradient after the applying of the observation time. Equation 26 describes the normalized signal incorporating the effect of an internal gradient:

$$\frac{S}{S_0} = exp\left\{-D_R\gamma^2\left[\delta^2\left(4\Delta + 6\lambda - \frac{2\delta}{3}\right)g_a^2 + 2\lambda\delta(\delta_1 - \delta_2)g_a g_0 + \frac{4}{3}\lambda^3 g_0^2\right]\right\} \quad 26$$

This sequence is repeated for a range of gradually increasing PFG strengths (g_a) and the measured echo signal intensity, S, is logged. Referring to Fig. 2, if the time interval between the first 180° pulse and the de-phasing PFG, δ_1 and the time interval between the de-phasing PFG and the second 90° pulse, δ_2, is equal, and the diffusion time, Δ, is much larger than the time interval between the two 90° pulses, λ, then the relationship between S and g_a is given by Eqn. 27 where S_o is the S in the absence of an applied PFG and γ is the gyromagnetic constant of hydrogen (2.68 × 108 (Ts)-1).

Theoretically, with the measured values of S and g_a, the restricted diffusion coefficient can be obtained from the gradient of the curve plotted using Eqn. 27. Consequently, this equation only holds true for the linear region of the attenuation curve, that is, as g_a approaches zero. This is because at higher applied field strengths, the curve begins to flatten out as the diffusing molecules have had a much longer time to probe the smallest micropores of the sample. As such, the resulting echo signal is dominated by the low diffusion coefficient occurring in the smallest pores and is not an accurate representation of the actual porous matrix. An analysis technique to extract the restricted diffusion coefficient from the gradient of the linear region of the attenuation curve is outlined next.

During the PFG NMR experiment, the intensity S is monitored as a function of applied magnetic field g. The PFG NMR experiment is usually performed for different diffusion times, Δ, to investigate the effects of restricted diffusion with an increasing Δ. The diffusion coefficients are calculated from the acquired signal attenuation plots using the following relation by choosing $\delta_1 = \delta_2$, the second term becomes equal to zero whereas the choosing of Δ should be much greater than λ leads in making the final term negligible in value and a constant if λ is also kept fixed. Equation 27 resulted from applying the previous mentioned modification into Eqn. 26:

$$\frac{S}{S_0} = exp\left\{-D_R\gamma^2\left[\delta^2\left(4\Delta + 6\lambda - \frac{2\delta}{3}\right)g_a^2\right]\right\} = exp(-b'D_R) \quad 27$$

The restricted diffusion coefficient is obtained by plotting signal attenuation vs. b, which has the applied magnetic field parameter as the variable term.

It is important to note that, in general, the PFG NMR method would overestimate the average pore size. This is due to the fact that the stimulated echo PFG NMR experiment is T_1 weighted, and at the longer observation times, signals from the smaller pores with relatively shorter T_1 would be lost. This is an important point that must be recognized when dealing with shaly or low permeability rocks. Subsequently, the T_1 bias of the average pore size is not expected to be very significant in the case of sandstone, which has relatively long T_1 distribution[53].

Methodology

Two Indiana limestone rocks with different permeability values were used in this study to evaluate the effect of permeability in estimating different tortuosity types for the same lithology. Petrophysical properties such as pore volume, porosity, and permeability of the core plugs using automated helium porosimeter-permeameter (AP-608) were tested. The automated permeameter can measure permeability at a very wide range from 0.001 md to 10,000 md at various confining pressures. Rock porosity and pore volume are usually measured using Boyl's law, while gas permeability is calculated by the use of the pressure decay curve since it needs to be corrected.

Table 1 lists the values of length, diameter, rock porosity, and permeability for the two limestone cores.

The micro-CT system has the significant advantage of being able to capture high-resolution images. This allows for the direct imaging of pore bodies and throats in a larger pore system such as reservoir samples. It was utilized to estimate geometric and hydraulic tortuosity using the software PerGeos (FEI-ThermoFisher) for image processing.

NMR experiments were carried out on a MARAN Oxford NMR spectrometer equipped with actively shielded X, Y, and Z gradient coils. The 13-interval BG-PFGSTE was used to reduce the effect of the internal gradient and to optimize the signal-to-noise ratio (SNR) at long observation times. Twenty-one gradient steps were acquired at each Δ. The gradient list covered the

Table 1 *The petrophysical parameters, including the electrical tortuosity values, of the two limestone core samples.*

Sample Name	Length (cm)	Diameter (cm)	φ (%)	k (md)
Indiana 1	4.47	3.80	10.81	0.73
Indiana 2	4.79	3.79	17.43	216.89

range from 0 G/cm to 33 G/cm with a spacing linear in g^2. The gradient duration, δ, was set to 1.5 seconds in all experiments and Δ ranged from 100 ms to 1,200 ms.

The T_2 measurements were carried out using CPMG pulse sequence with echo spacing time = 0.114 ms and keeping the minimum SNR = 100.

Results and Discussion

The geometric tortuosity values of both Indiana limestone samples are computed using the centroid path method. The effective pore path is measured by determining the coordinate (x,y,z) of the pore centroid after determining the layer, and then connecting the pore centroid into a connected channel. Figures 4 and 5 show the extracted pore network model extracted from the micro-CT images used to compute the geometric and hydraulic tortuosity. These 3D pore network models were done at two different voxel resolutions based on the permeability of the sample to capture all possible pores of the samples.

Indiana 1 was scanned at a voxel resolution of 1.53 µm while Indiana 2 was scanned at a voxel resolution of 3.50 µm. The geometric tortuosity values obtained were 4.29 and 2.32 from Indiana 1 and Indiana 2, respectively. The values are higher than the values obtained in a previous study[54] using centroid path method, however, they studied only homogenous Fontainebleau sandstone at a maximum resolution of 4.38 µm. They showed that increasing the voxel resolution would increase the geometric tortuosity value. Furthermore, our samples here are carbonate and heterogeneous with a much more complex pore structure that would have higher geometric tortuosity values.

Fluid flow simulations were run to compute to hydraulic tortuosity values by analyzing the streamline identified from the pore-scale simulation on the extracted pore network model. Here, we estimated the effective path of the hydraulic flow by taking a weighted average of the streamline paths. The hydraulic tortuosity values showed lower values than the geometric tortuosity with a value of 2.25 for Indiana 1 and 1.78 for Indiana 2. The computed hydraulic tortuosity values indicate that the higher permeability sample's (Indiana 1) effective streamline path is shorter than the low permeability sample (Indiana 2). This is expected because in Kozeny-Carman equation the permeability is inversely proportional to the hydraulic tortuosity.

The electrical tortuosity, τ_e, was calculated for all samples using Eqn. 23. The equation inputs require resistivity of saturating fluid (brine), resistivity of the sample when it is 100% saturated with water, and the sample porosity. The electrical tortuosity measurements also confirmed that Indiana 2 is less tortuous than Indiana 1. Indiana 2 showed an electrical tortuosity value of 2.64, while Indiana 1 showed 3.07 of electrical tortuosity.

Figure 6 shows the T_2 relaxation time distribution for the carbonate samples studied. These distribution results confirm the petrophysical properties in Table 1 measured using the conventional techniques. Indiana 2 shows the longest T_2 relaxation distribution (bimodal system) with a peak value of 501.2 ms. In addition, the distribution predicts two connected pore size systems with fluid distributed approximately between the two pore systems, which can be seen from the pore network model in Fig. 4. The lowest permeability and porosity values of Indiana 1 were confirmed by the lower T_2, with a peak value of 79.4 ms. Furthermore, the widespread distribution of Indiana T_2 (10^{-4} s to ~1 s) indicates the

Fig. 4 *The 3D pore network model for Indiana 1.*

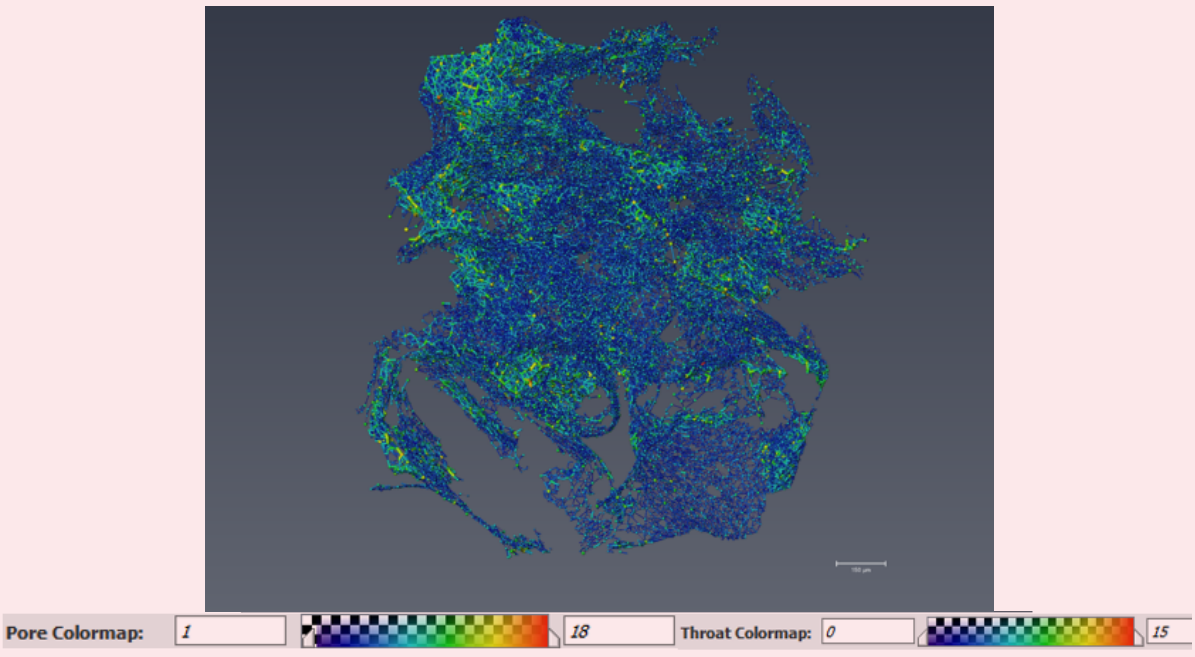

Fig. 5 *The 3D pore network model for Indiana 2.*

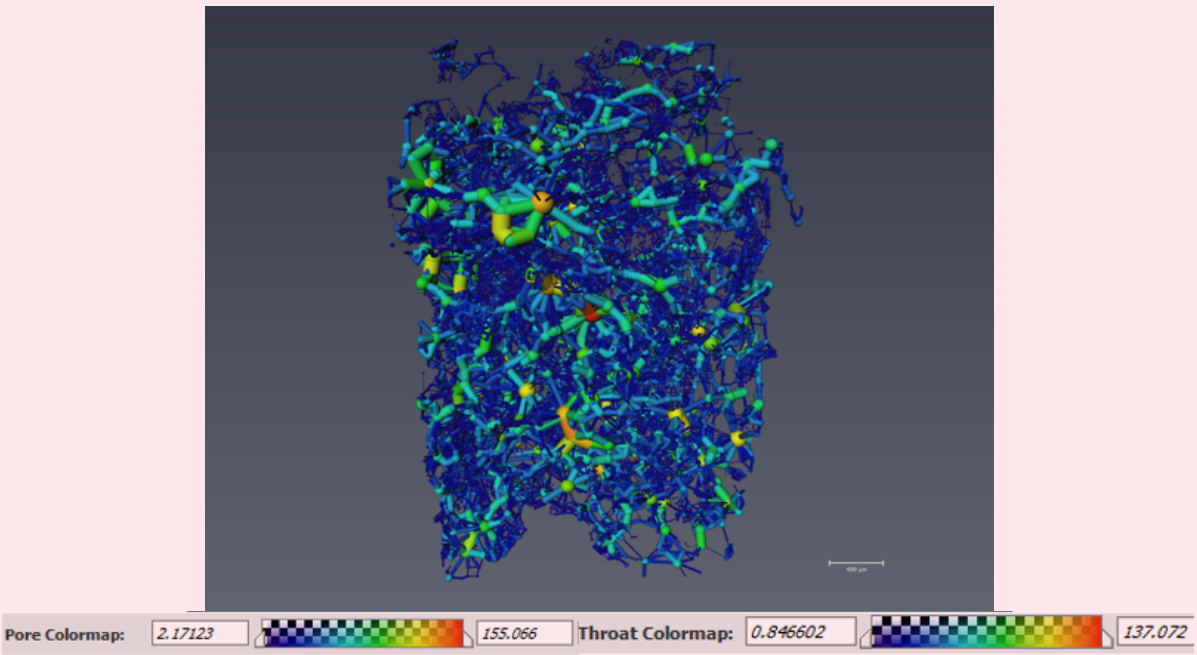

existing with different pore sizes with a complex pore structure.

The PFG NMR diffusion measurements were performed for the two rock core samples. A Matlab code was used to extract the RiD of files from the Oxford Instruments Maran DRX-HF spectrometer and convert it into files readable by the code.

Figure 7 shows the PFG NMR signal attenuation normalized data for the bulk brine. These data were acquired using the 13 interval BG-PFGSTE. The bulk fluid's measurements could be done using the simple PFG NMR instead of a PFGSTE, however, a PFGSTE is performed to have a comparable result with restricted diffusion data. The experiment showed a very good SNR and all the data fit accurately. The self-diffusion coefficient, D, of brine, i.e., not in the rock core, was measured in a glass vial that has a minimum ^{1}H NMR signal. This was determined to be 2.37×10^{-9} m^2/s and was found to be consistent with other literature[34, 55, 56].

The restricted diffusion of both samples was measured at different diffusion times until there is no change in the restricted diffusion coefficient value. This asymptotic value corresponds to the inverse of diffusion tortuosity. Figure 8 shows the D_R/D_0 as a function of the diffusion time for both rock core samples used in this study. It can be seen that at a specific diffusion time, the restricted diffusion coefficient of Indiana 1 is lower than Indiana 2, which indicates a more restricted pore space. As observed in the other tortuosity types, the diffusion tortuosity of Indiana 1 showed a higher value (7.80) than the one obtained for Indiana 2 (4.92).

Table 2 lists the values of all different tortuosity types for Indiana 1 and Indiana 2 samples. The diffusion tortuosity showed the highest values among the different types for both samples. Furthermore, the lowest tortuosity values were observed in the hydraulic tortuosity measures. Electrical and geometric tortuosity ranged between the values of the hydraulic and diffusion tortuosity.

Fig. 6 *The T_2 relaxation distribution for both samples.*

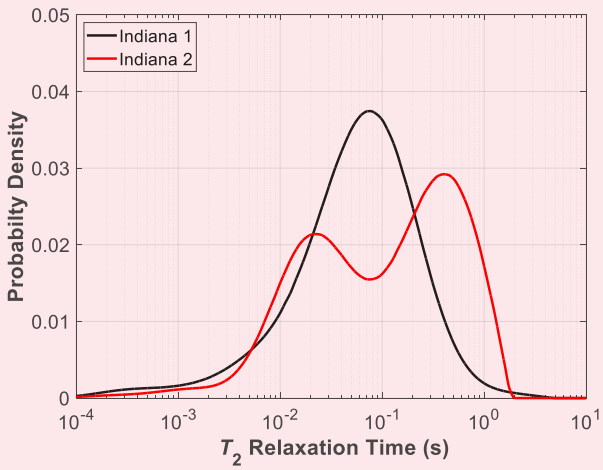

Conclusions

Micro-CT, a four electrode configuration, and PFG NMR techniques were performed to evaluate the different tortuosity types of two carbonate samples. Generally, a

high permeability carbonate sample (Indiana 2) showed lower tortuosity values using different techniques than the low permeability sample (Indiana 1).

The PFG NMR diffusion tortuosity values demonstrate the highest tortuosity values among all types while the hydraulic tortuosity values showed the lowest values.

Fig. 7 *The PFG NMR signal attenuation of brine showing the self-diffusion coefficient as the slope of the fitted curve.*

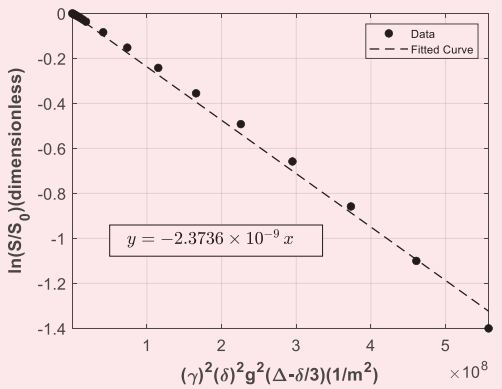

Fig. 8 *The DR/D0 as a function of the diffusion time for both samples.*

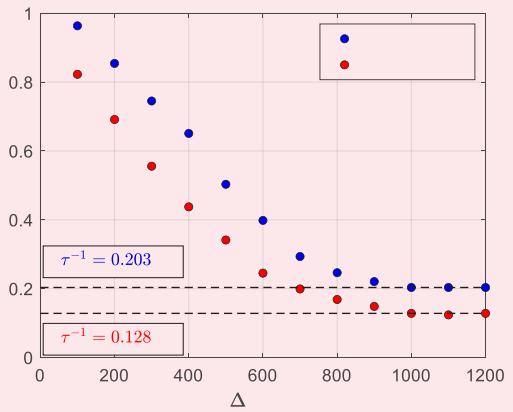

Table 2 *The different tortuosity type values of both Indiana limestone samples used in this study.*

Sample Name	τ_g	τ_h	τ_e	τ_d
Indiana 1	4.29	2.25	3.07	7.80
Indiana 2	2.32	1.78	2.64	4.92

References

1. Blunt, M.J., Bijeljic, B., Dong, H., Gharbi, O., et al.: "Pore-Scale Imaging and Modeling," *Advances in Water Resources*, Vol. 51, January 2013, pp. 197-216.
2. Bultreys, T., De Boever, W. and Cnudde, V.: "Imaging and Image-Based Fluid Transport Modeling at the Pore Scale in Geological Materials: A Practical Introduction to the Current State-of-the-Art," *Earth-Science Reviews*, Vol. 155, April 2016, pp. 93-128.
3. Adler, P.M., Jacquin, C.G. and Quiblier, J.A.: "Flow in Simulated Porous Media," *International Journal of Multiphase Flow*, Vol. 16, Issue 4, July-August 1990, pp. 691-712.
4. Srisutthiyakorn, N. and Mavko, G.M.: "What is the Role of Tortuosity in the Kozeny-Carman Equation?" *Interpretation*, Vol. 5, Issue 1, February 2017, pp. SB57-SB67.
5. Bae, C-J., Erdonmez, C.K., Halloran, J.W. and Chiang, Y-M.: "Design of Battery Electrodes with Dual-Scale Porosity to Minimize Tortuosity and Maximize Performance," *Advanced Materials*, Vol. 25, Issue 9, March 2013, pp. 1254-1258.
6. Zacharias, N.A., Nevers, D.R., Skelton, C., Knackstedt, K., et al.: "Direct Measurements of Effective Ionic Transport in Porous Li-Ion Electrodes," *Journal of the Electrochemical Society*, Vol. 160, Issue 2, December 2012, pp. A306-A311.
7. Karanikola, V., Corral, A.F., Jiang, H., Sáez, A.E., et al.: "Effects of Membrane Structure and Operational Variables on Membrane Distillation Performance," *Journal of Membrane Science*, Vol. 524, February 2017, pp. 87-96.
8. Bini, F., Pica, A., Marinozzi, A. and Marinozzi, F.: "A 3D Model of the Effect of Tortuosity and Constrictivity on the Diffusion in Mineralized Collagen Fibril," *Scientific Reports*, Vol. 9, Issue 1, February 2019.
9. Botchwey, E.A., Dupree, M.A., Pollack, S.R., Levine, E.M., et al.: "Tissue Engineered Bone: Measurement of Nutrient Transport in Three-Dimensional Matrices," *Journal of Biomedical Materials Research*, Vol. 67, Issue 1, October 2003, pp. 357-367.
10. Ghanbarian, B., Hunt, A.G., Ewing, R.P. and Sahimi, M.: "Tortuosity in Porous Media: A Critical Review," *Soil Science Society of America Journal*, Vol. 77, Issue 5, September-October 2013, pp. 1461-1477.
11. Adler, P.M.: *Porous Media: Geometry and Transports*, Elsevier, 1992, 560 p.
12. Schlüter, S., Sheppard, A., Brown, K. and Wildenschild, D.: "Image Processing of Multiphase Images Obtained via X-ray Microtomography: A Review," *Water Resources Research*, Vol. 50, Issue 4, April 2014, pp. 3615-3639.
13. Stutzman, P.: "Scanning Electron Microscopy Imaging of Hydraulic Cement Microstructure," *Cement and Concrete Composites*, Vol. 26, Issue 8, November 2004, pp. 957-966.
14. Sun, H., Vega, S., Tao, G., Yong, H., et al.: "Estimation of Petrophysical Parameters of Heterogeneous Carbonate Rock Sample with Multi-Scale CT Images," SPE paper 183114, presented at the Abu Dhabi International Petroleum Exhibition and Conference, Abu Dhabi, UAE, November 7-10, 2016.
15. Thovert, J.F., Salles, J. and Adler, P.M.: "Computerized Characterization of the Geometry of Real Porous Media: Their Discretization, Analysis and Interpretation," *Journal of Microscopy*, Vol. 170, Issue 1, April 1993, pp. 65-79.
16. Sun, W.C., Andrade, J.E. and Rudnicki, J.W.: "Multiscale Method for Characterization of Porous Microstructures

and their Impact on Macroscopic Effective Permeability," *International Journal for Numerical Methods in Engineering*, Vol. 88, Issue 12, December 2011, pp. 1260-1279.

17. Jørgensen, P.S., Hansen, K.V., Larsen, R. and Bowen, J.R.: "Geometrical Characterization of Interconnected Phase Networks in Three Dimensions," *Journal of Microscopy*, Vol. 244, Issue 1, October 2011, pp. 45-58.

18. Sobieski, W., Matyka, M., Gołembiewski, J. and Lipiński, S.: "The Path Tracking Method as an Alternative for Tortuosity Determination in Granular Beds," *Granular Matter*, Vol. 20, Issue 4, September 2018.

19. Clennell, M.B.: "Tortuosity: A Guide through the Maze," *Geological Society, London, Special Publications*, Vol. 122, January 1997, pp. 299-344.

20. Duda, A., Koza, Z. and Matyka, M.: "Hydraulic Tortuosity in Arbitrary Porous Media Flow," *Physical Review E*, Vol. 84, Issue 3, September 2011.

21. Berg, C.F.: "Permeability Description by Characteristic Length, Tortuosity, Constriction and Porosity," *Transport in Porous Media*, Vol. 103, Issue 3, April 2014, pp. 381-400.

22. Wylie, M.R.J. and Spangler, M.B.: "Application of Electrical Resistivity Measurements to Problem of Fluid Flow in Porous Media," *Bulletin of the American Association of Petroleum Geologists*, Vol. 36, Issue 2, February 1952, pp. 359-403.

23. Berg, C.F.: "Reexamining Archie's Law: Conductance Description by Tortuosity and Constriction," *Physical Review E*, Vol. 86, Issue 4, October 2012.

24. Ramirez, A., Daily, W., Binley, A., LaBrecque, D., et al.: "Detection of Leaks in Underground Storage Tanks Using Electrical Resistance Methods," *Journal of Environmental and Engineering Geophysics*, Vol. 1, Issue 3, December 1996, pp. 189-203.

25. Keller, G.V.: "Electrical Properties of Sandstones of the Morrison Formation," in *Trace Elements Investigations 592*, 1957, 64 p.

26. Archie, G.E.: "The Electrical Resistivity Log as an Aid in Determining Some Reservoir Characteristics," *Transactions of the AIME*, Vol. 146, Issue 1, December 1942, pp. 54-62.

27. Saner, S., Al-Harthi, A. and Htay, M.T.: "Use of Tortuosity for Discriminating Electrofacies to Interpret the Electrical Parameters of Carbonate Reservoir Rocks," *Journal of Petroleum Science and Engineering*, Vol. 16, Issue 4, December 1996, pp. 237-249.

28. Salem, H.S. and Chilingarian, G.V.: "The Cementation Factor of Archie's Equation for Shaly Sandstone Reservoirs," *Journal of Petroleum Science and Engineering*, Vol. 23, Issue 2, August 1999, pp. 83-93.

29. Cornell, D. and Katz, D.L.: "Flow of Gases through Consolidated Porous Media," *Industrial & Engineering Chemistry*, Vol. 45, Issue 10, 1953, pp. 2145-2152.

30. Perez-Rosales, C.: "Generalization of the Maxwell Equation for Formation Resistivity Factors (includes associated papers 6556 and 6557)," *Journal of Petroleum Technology*, Vol. 28, Issue 7, July 1976, pp. 819-824.

31. Chen, S., Miao, P.M. and Watson, A.T.: "Characterization of Pore Structures Using NMR Restricted Diffusion Measurements," SPE paper 24812, presented at the SPE Annual Technical Conference and Exhibition, Washington, D.C., October 4-7, 1992.

32. Tutunjian, P.N., Vinegar, H.J., Ferris, J.A. and Nesbitt, G.J.: "Characterization of Pore Microgeometry by NMR Diffusion Measurements," paper presented at the SPWLA 34th Annual Logging Symposium, Calgary, Alberta, Canada, June 13-16, 1993.

33. Anand, V. and Hirasaki, G.J.: "Paramagnetic Relaxation in Sandstones: Distinguishing T_1 and T_2 Dependence on Surface Relaxation, Internal Gradients and Dependence on Echo Spacing," *Journal of Magnetic Resonance*, Vol. 190, Issue 1, January 2008, pp. 68-85.

34. Hürlimann, M.D.: "Effective Gradients in Porous Media due to Susceptibility Differences," *Journal of Magnetic Resonance*, Vol. 131, Issue 2, April 1998, pp. 232-240.

35. Hürlimann, M.D., Helmer, K.G., Latour, L.L. and Sotak, C.H.: "Restricted Diffusion in Sedimentary Rocks. Determination of Surface Area-to-Volume Ratio and Surface Relaxtivity," *Journal of Magnetic Resonance, Series A*, Vol. 111, Issue 2, December 1994, pp. 169-178.

36. Latour, L.L., Kleinberg, R.L., Mitra, P.P. and Sotak, C.H.: "Pore-Size Distributions and Tortuosity in Heterogeneous Porous Media," *Journal of Magnetic Resonance, Series A*, Vol. 112, Issue 1, January 1995, pp. 83-91.

37. Mair, R.W., Wong, G.P., Hoffmann, D., Hürlimann, M.D., et al.: "Probing Porous Media with Gas Diffusion NMR," *Physical Review Letters*, Vol. 83, Issue 16, October 1999, pp. 3324-3327.

38. Mair, R.W., Hürlimann, M.D., Sen, P.N., Schwartz, L.M., et al.: "Tortuosity Measurement and the Effects of Finite Pulse Widths on Xenon Gas Diffusion NMR Studies of Porous Media," *Magnetic Resonance Imaging*, Vol. 19, Issues 3-4, April-May 2001, pp. 345-351.

39. Wang, R., Pavlin, T., Rosen, M.S., Mair, R.W., et al.: "Xenon NMR Measurements of Permeability and Tortuosity in Reservoir Rocks," *Magnetic Resonance Imaging*, Vol. 23, Issue 2, February 2005, pp. 329-331.

40. Frosch, G.P., Tillich, J.E., Haselmeier, R., Holz, M., et al.: "Probing the Pore Space of Geothermal Reservoir Sandstones by Nuclear Magnetic Resonance," *Geothermics*, Vol. 29, Issue 6, December 2000, pp. 671-687.

41. Yang, K., Li, M., Ling, N.N.A., May, E.F., et al.: "Quantitative Tortuosity Measurements of Carbonate Rocks Using Pulsed Field Gradient NMR," *Transport in Porous Media*, Vol. 130, December 2019, pp. 847-865.

42. Sen, P.N.: "Time-Dependent Diffusion Coefficient as a Probe of Geometry," *Concepts in Magnetic Resonance Part A: Bridging Education and Research*, Vol. 23A, Issue 1, September 2004, pp. 1-21.

43. Callaghan, P.T., Coy, A., MacGowan, D., Packer, K.J., et al.: "Diffraction-like Effects in NMR Diffusion Studies of Fluids in Porous Solids," *Nature*, Vol. 351, June 1991, pp. 467-469.

44. Mitchell, J., Chandrasekera, T.C., Johns, M.L., Gladden, L.F., et al.: "Nuclear Magnetic Resonance Relaxation and Diffusion in the Presence of Internal Gradients: The Effect of Magnetic Field Strength," *Physical Review E*, Vol. 81, Issue 2, February 2010.

45. Stejskal, E.O. and Tanner, J.E.: "Spin Diffusion Measurements: Spin Echoes in the Presence of a Time-Dependent Field Gradient," *The Journal of Chemical Physics*, Vol. 42, Issue 1, January 1965, pp. 288-292.

46. Price, W.S: *NMR Studies of Translational Motion (Principles and Applications)*, Cambridge University Press, July 2009, 416 p.

47. Willis, S.A., Stait-Gardner, T.J., Torres, A.M. and Price, W.S.: "Fundamentals of Diffusion Measurements Using NMR," Chapter 2 in *Diffusion NMR of Confined Systems: Fluid Transport in Porous Solids and Heterogeneous Materials*, The Royal Society of Chemistry, 2017, pp. 16-51.

48. Price, W.S.: "Pulsed-Field Gradient Nuclear Magnetic Resonance as a Tool for Studying Translational Diffusion: Part II. Experimental Aspects," *Concepts in Magnetic Resonance*, Vol. 10, Issue 4, December 1998, pp. 197-237.

49. Cotts, R.M., Hoch, M.J.R., Sun, T. and Markert, J.T.: "Pulsed Field Gradient Stimulated Echo Methods for Improved NMR Diffusion Measurements in Heterogeneous Systems," *Journal of Magnetic Resonance*, Vol. 83, Issue 2, June 1989, pp. 252-266.

50. Elsayed, M., Mahmoud, M., El-Husseiny, A., Kamal, M.S., at el.: "A New Method to Evaluate Reaction Kinetics of Acids with Carbonate Rocks Using NMR Diffusion Measurements," *Energy & Fuels*, Vol. 34, Issue 1, December 2019, pp. 787-797.

51. Zecca, M., Vogt, S.J., Connolly, P.R.J., May, E.F., et al.: "NMR Measurements of Tortuosity in Partially Saturated Porous Media," *Transport in Porous Media*, Vol. 125, Issue 2, July 2018, pp. 271-288.

52. Appel, M., Freeman, J.J., Perkins, R.B. and Hofman, J.P.: "Restricted Diffusion and Internal Field Gradients," paper presented at the SPWLA 40th Annual Logging Symposium, Oslo, Norway, May 30-June 3, 1999.

53. Mitchell, J.: "Industrial Applications of Magnetic Resonance Diffusion and Relaxation Time Measurements," Chapter 11 in *Diffusion NMR of Confined Systems: Fluid Transport in Porous Solids and Heterogeneous Materials*, The Royal Society of Chemistry, 2017, pp. 353-389.

54. Fu, J., Thomas, H.R. and Li, C.: "Tortuosity of Porous Media: Image Analysis and Physical Simulation," *Earth-Science Reviews*, Vol. 212, January 2021.

55. Elsayed, M., Glatz, G., El-Husseiny, A., Alqubalee, A., et al.: "The Effect of Clay Content on the Spin-Spin NMR Relaxation Time Measured in Porous Media," *ACS Omega*, Vol. 5, Issue 12, March 2020, pp. 6545-6555.

56. Zhang, G.Q., Hirasaki, G.J. and House, W.V.: "Internal Field Gradients in Porous Media," *Petrophysics*, Vol. 44, Issue 6, November 2003, pp. 422-434.

About the Authors

Dr. Hyung T. Kwak

Ph.D. in Physical Chemistry, Ohio State University

Dr. Hyung T. Kwak joined Saudi Aramco in April 2010 as a Petroleum Engineer with Saudi Aramco's Exploration and Petroleum Engineering Center – Advance Research Center (EXPEC ARC). He had been a member of the Pore Scale Physics focus area (2010 to 2012) and SmartWater Flooding focus area (2013 to 2014) of the Reservoir Engineering Technology Division. Currently, Hyung is a focus area champion of the Pore Scale Physics focus area. His main research focus is seeking deeper understanding of fluid-rock interaction in pore scale of the Kingdom's reservoirs.

Since joining Saudi Aramco in 2010, Hyung has been involved with various improved oil recovery and enhanced oil recovery (EOR) research projects, such as SmartWater Flooding, carbon dioxide EOR, and chemical EOR. Prior to joining Saudi Aramco, Hyung was a Research Scientist at Baker Hughes, with a main area of research related to nuclear magnetic resonance (NMR)/ magnetic resonance imaging technology.

In 1996, Hyung received a B.S. degree in Chemistry from the University of Pittsburgh, Pittsburgh, PA, and in 2001, he received his Ph.D. degree in Physical Chemistry from Ohio State University, Columbus, Ohio.

Before moving into the oil and gas industry, Hyung was involved — as a postdoctoral fellow for 2 years — in a project developing the world's largest wide bore superconducting magnet NMR spectrometer, 900 MHz, at the National High Magnetic Field Laboratory.

He has more than 100 publications, including peer-reviewed articles and patents.

Mahmoud Elsayed

M.S. in Petroleum Engineering, King Fahd University of Petroleum and Minerals

Mahmoud Elsayed is currently working as a Laboratory Specialist in the Laboratories Technical Support & Services Department at the College of Petroleum Engineering & Geoscience. He has done extensive training in the University of Western Australia in advanced nuclear magnetic resonance (NMR) rock core analysis techniques — specifically diffusion and propagator measurements. Mahmoud's main research interest is focused on the application of NMR in petroleum engineering.

He is actively participating in research and providing training to graduate students and Saudi Aramco's NMR laboratory personnel on NMR experiments. Mahmoud is the author and coauthor of several peer-reviewed journal articles.

He received both his B.S. degree and M.S. degree in Petroleum Engineering from King Fahd University of Petroleum and Minerals (KFUPM), Dhahran, Saudi Arabia.

Dr. Ammar El-Husseiny

Ph.D. in Geophysics, Stanford University

Dr. Ammar El-Husseiny is an Assistant Professor of Geophysics at King Fahd University of Petroleum and Minerals (KFUPM), Dhahran, Saudi Arabia. Before joining KFUPM, he worked as a research and teaching associate in the Petroleum Institute of Abu Dhabi, UAE.

Ammar's main research interest is focused on the rock physics of carbonates characterizing their transport and elastic properties. Other topics of interest also include: investigating the feasibility and the interpretation of time-lapse seismic in carbonates, as well as the use of nuclear magnetic resonance for advanced petrophysics applications.

He received his B.S. degree in Petroleum Geosciences from KFUPM. Ammar received both his M.S. degree and Ph.D. degree in Geophysics from Stanford University, Stanford, CA.

Dr. Mohamed Mahmoud

Ph.D. in Petroleum Engineering, Texas A&M University

Dr. Mohamed Mahmoud is a Professor working in the Department of Petroleum Engineering at King Fahd University of Petroleum and Minerals (KFUPM), Dhahran, Saudi Arabia. His areas of research include carbonate and sandstone stimulation, formation damage, and rock petrophysics and geomechanics.

Mohamed has authored or coauthored several journal and conference papers, in addition to more than 80 U.S. patents.

He received both his B.S. degree and M.S. degree in Petroleum Engineering from Suez Canal University, Ismailia, Egypt. Mohamed received his Ph.D. degree in Petroleum Engineering from Texas A&M University, College Station, TX, in 2011.